Multifractal spectral features enhance classification of anomalous diffusion

Henrik Seckler [1], Ralf Metzler [1,2,*], Damian G. Kelty-Stephen,[3] and Madhur Mangalam [4,†]

[1]*Institute for Physics & Astronomy, University of Potsdam, 14476 Potsdam-Golm, Germany*
[2]*Asia Pacific Center for Theoretical Physics, Pohang 37673, Republic of Korea*
[3]*Department of Psychology, State University of New York at New Paltz, New Paltz, New York 12561, USA*
[4]*Department of Biomechanics and Center for Research in Human Movement Variability,*
University of Nebraska at Omaha, Omaha, Nebraska 68182, USA

Anomalous diffusion processes, characterized by their nonstandard scaling of the mean-squared displacement, pose a unique challenge in classification and characterization. In a previous study [Mangalam *et al.*, Phys. Rev. Res. **5**, 023144 (2023)], we established a comprehensive framework for understanding anomalous diffusion using multifractal formalism. The present study delves into the potential of multifractal spectral features for effectively distinguishing anomalous diffusion trajectories from five widely used models: fractional Brownian motion, scaled Brownian motion, continuous-time random walk, annealed transient time motion, and Lévy walk. We generate extensive datasets comprising 10^6 trajectories from these five anomalous diffusion models and extract multiple multifractal spectra from each trajectory to accomplish this. Our investigation entails a thorough analysis of neural network performance, encompassing features derived from varying numbers of spectra. We also explore the integration of multifractal spectra into traditional feature datasets, enabling us to assess their impact comprehensively. To ensure a statistically meaningful comparison, we categorize features into concept groups and train neural networks using features from each designated group. Notably, several feature groups demonstrate similar levels of accuracy, with the highest performance observed in groups utilizing moving-window characteristics and p variation features. Multifractal spectral features, particularly those derived from three spectra involving different timescales and cutoffs, closely follow, highlighting their robust discriminatory potential. Remarkably, a neural network exclusively trained on features from a single multifractal spectrum exhibits commendable performance, surpassing other feature groups. In summary, our findings underscore the diverse and potent efficacy of multifractal spectral features in enhancing the predictive capacity of machine learning to classify anomalous diffusion processes.

I. INTRODUCTION

Anomalous diffusion is a ubiquitous phenomenon found in diverse natural settings, including atoms confined in magneto-optical traps [1,2]; the behavior of various biological entities such as DNA, lipids, and proteins [3–12]; microorganisms like bacteria, cells, and parasites [13–20]; as well as in the behavior of foraging wild animals [21–23] and even among human hunter-gatherer societies [24,25]. Anomalous diffusion manifests itself in economic markets [26–28] and a wide array of other processes [29–33], and it exhibits characteristics that span multiple temporal and spatial scales. In these processes, there is a distinctive, erratic evolution of an observable property (e.g., position, temperature, or stock price) over time. The term "anomalous" signifies that the mean-squared displacement (MSD) of the observable x does not follow a linear growth with time t as predicted by Fick's theory of diffusion but rather adheres to the more general power-law behavior,

$$\langle x^2(t) \rangle \propto t^\beta, \tag{1}$$

where the anomalous exponent $\beta \neq 1$. For example, $\beta = 1$ corresponds to the linear growth observed in Brownian motion [34,35]. Frequently, one observes $\beta < 1$, indicating subdiffusion [6,16,36–47], while superdiffusion, characterized by $\beta > 1$, is less commonly observed but can be found in active physical and biological systems [48–57].

One of the primary motivations for investigating anomalous diffusion models is identifying and categorizing specific anomalous diffusion phenomena in real-world data. Nevertheless, the complexities outlined above render this classification a formidable challenge. As a result, recent endeavors have encompassed Bayesian methodologies [58–62], as well as machine-learning (ML) strategies [63–73], and even unsupervised techniques [74,75]. However, these approaches often rely on atheoretical features, which may not correspond to plausible generative mechanisms [73,76,77]. A more theoretically grounded feature set can enhance the ML-based characterization of anomalous diffusion processes within empirical data.

In a previous study [78], we took an initial stride towards establishing a comprehensive framework rooted in understanding anomalous diffusion using the multifractal formalism [79–81] aimed at re-establishing ergodicity within

*rmetzler@uni-potsdam.de
†mmangalam@unomaha.edu

the description of anomalous-diffusion phenomena [82–84]. We harnessed synthetic data that mirror a wide spectrum of anomalous-diffusion processes, spanning various values of the anomalous exponent β. These processes, encompassing both ergodic and nonergodic behaviors, were approximated through five distinct mathematical models: fractional Brownian motion (FBM, ergodic), scaled Brownian motion (SBM, weakly nonergodic), continuous-time random walk (CTRW, weakly nonergodic), annealed transient time motion (ATTM, weakly nonergodic), and Lévy walk (LW, ultraweakly nonergodic). Our investigation revealed that descriptors linked to the time-averaged and ensemble-averaged mean-squared displacement (TAMSD and MSD), including linear metrics such as standard deviation, coefficient of variation, and root mean square, exhibit a disruption of ergodicity. In stark contrast, descriptors addressing the temporal structure and potential nonlinearity, such as multifractality and, to a certain extent, fractality, display time-independent behavior, functioning as ergodic descriptors insensitive to the minor ergodicity deviations inherent to these processes. Consequently, these descriptors provide consistent information across various diffusion processes and anomalous exponents β. Further analysis traced back these patterns to the multiplicative cascades underpinning these diffusion phenomena, as the multifractal spectrum's shape and symmetry, in conjunction with those of corresponding surrogate series, distinguish these processes.

This previous work [78] has opened the door to the potential use of multifractal spectral (MFS) features in improving the classification of anomalous diffusion. Multifractal geometry provides a formalism explicitly tailored to address the intermittent, nonergodic fluctuations that manifest themselves across multiple space- and timescales, encompassing the intricate interplay between short-range events and large-scale contextual factors [85,86]. This perspective does not imply that the underlying models generating these diverse forms of anomalous diffusion are inherently multifractal. Instead, it recognizes multifractal geometry as a versatile modeling framework with a long-standing history of explaining how these modes of anomalous diffusion evolve, occasionally transitioning between different regimes [87]. Given the successful application of multifractal geometrical estimations as ergodic descriptors in previous work for various anomalous diffusion processes, incorporating MFS features alongside traditional feature sets in ML models holds promise for enhancing the classification of anomalous diffusion.

In this investigation, we delve into the potential of MFS features for discerning anomalous-diffusion patterns. Our approach begins by generating datasets comprising trajectories derived from five distinct anomalous diffusion models—FBM, SBM, CTRW, ATTM, and LW. From each trajectory, we extract multiple multifractal spectra. Our analysis encompasses assessing a neural network's performance when trained on features derived from varying numbers of spectra. Furthermore, we explore the augmentation of datasets containing traditional features, as documented in previous works [69,76], with multifractal spectra. To culminate the study, we categorize features into distinct concept groups and gauge the performance of each group; this categorization enables a

meaningful comparison against the novel concept introduced herein—MFS features.

The paper follows a structured sequence. Beginning with a concise introduction to the employed dataset, traditional features, multifractal analysis, and the machine learning model in Sec. II, we assess the performance of MFS features in Sec. III. This encompasses the outcomes achieved by utilizing MFS features independently, alongside, or in contrast to traditional feature sets. The paper concludes with a comprehensive discussion and a glimpse into avenues for future research in Sec. IV.

II. METHODS

A. Diffusion models and dataset

To ensure comparability, our dataset generation process closely aligns with that employed in the *Anomalous-Diffusion-(AnDi-) Challenge* [70,71,88]. Nevertheless, it is noteworthy that, in contrast to the AnDi-Challenge dataset, we focus solely on trajectories within the $250 \leqslant N < 1000$ range, where N is the number of datapoints. This omission of shorter trajectories is necessitated by the specific constraints associated with the features utilized in our study. Considering trajectories within $250 \leqslant N < 1000$ does not influence ergodicity breaking, as this phenomenon depends on the underlying dynamics rather than the length of the trajectory. Each trajectory is randomly assigned to one of five distinct diffusion models; all yield anomalous diffusion patterns conforming to Eq. (1). We present sample trajectories for each in Figs. 1(a) and 1(c), which show the time evolution of the position of a particle diffusing according to each of the five anomalous diffusion models for different values of β. Figures 1(b) and 1(d) shows the extracted multifractal spectra for each of these trajectories (see Sec. II C).

These diffusion processes show differences in how increments are generated, corresponding to distinct statistical mechanisms of anomalous diffusion (see Appendix A).

We generated a dataset comprising 10^6 trajectories using the `andi-datasets` [75] Python package. These trajectories have a range of randomly selected anomalous exponents β, with values $\beta \in \{0.05, 0.10, \ldots, 1.95, 2\}$, albeit with some variations based on the specific model. Particularly, the CTRW and ATTM models exhibit only sub- and normal-diffusive behaviors ($\beta \leqslant 1$), while the LW model is exclusively superdiffusive ($\beta > 1$) and even ballistic ($\beta = 2$). Additionally, this dataset does not consider ballistic ($\beta = 2$) FBM. To simulate conditions more akin to experimental data, we introduced additive white Gaussian noise ξ_n to all trajectories at varying levels, resulting in signal-to-noise ratios (snr) of 0.1, 0.5, or 1. Given a trajectory $\tilde{x}_n$, we obtain the noisy trajectory $x_n = \tilde{x}_n + \xi_n$ with the superimposed noise

$$\xi_n \sim \frac{\sigma_{\Delta\tilde{x}}}{\text{snr}} \mathcal{N}(0, 1), \tag{2}$$

where $\sigma_{\Delta\tilde{x}}$ is the standard deviation of the unperturbed increment process $\Delta\tilde{x}_n = \tilde{x}_{n+1} - \tilde{x}_n$.

Of the 10^6 trajectories, 9×10^5 (90%) were allocated for training the ML algorithms. The remaining 10^5 trajectories
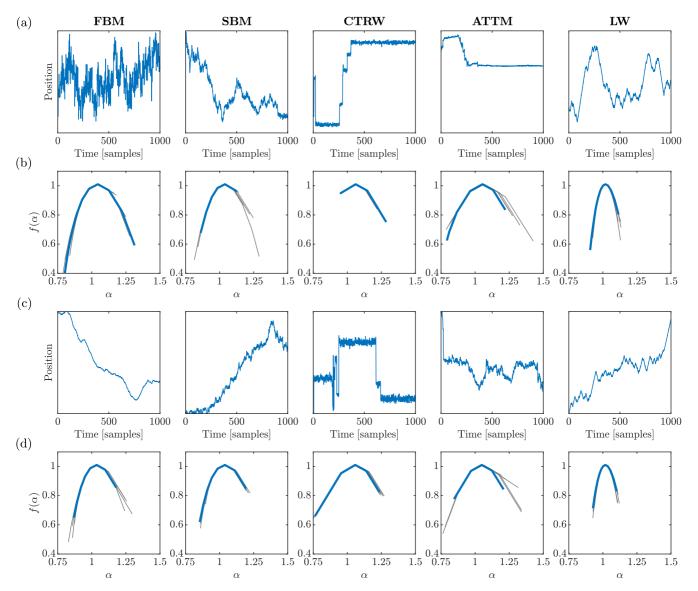
FIG. 1. Representative trajectories of the five anomalous diffusion processes for various anomalous exponents [(a) and (c)] and the respective multifractal spectrum [(b) and (d)]. The spectrum in blue (bold) corresponds to the original time series, while the spectra in gray correspond to five IAAFT surrogates.

(10%) were evenly divided into a validation set to refine the training parameters and a separate test set to evaluate the performance metrics reported in this study.

B. Traditional features

The traditional features considered for anomalous diffusion classification encompassed many parameters based on Ref. [69], as listed in Table I. Appendix B provides definitions and mathematical details for each feature (see also Ref. [69]).

C. Multifractal spectral features

We used Chhabra and Jensen's [89] direct method for all analyses of this section. This method estimates the multifractal spectrum width $\Delta\alpha$ by sampling a series x_k at progressively longer scales using the proportion $P_v(n)$ of the signal falling within the vth bin of length n as

$$P_v(n) = \frac{\sum_{k=(v-1)n+1}^{v \cdot n} x_k}{\sum_{k=1}^{N} x_k}, \quad n = \{4, 8, 16, \dots\} \langle N_{\max}. \quad (3)$$

As n increases, $P_v(n)$ represents a progressively larger proportion of $x(t)$,

$$P(n) \propto n^\alpha, \quad (4)$$

suggesting a growth of the proportion according to one "singularity" strength α [90]. $P(n)$ exhibits multifractal dynamics when it grows heterogeneously across timescales n according to multiple singularity strengths, such that

$$P(n_v) \propto n^{\alpha_v}, \quad (5)$$

TABLE I. Traditional features considered for anomalous diffusion classification based on Ref. [69]. See Appendix B or Ref. [69] for detailed definitions.

Anomalous exponent
Diffusion coefficient
Efficiency
Empirical velocity autocorrelation function
Fractal dimension
Maximal excursion
Mean maximal excursion
Kurtosis
Mean Gaussianity
Mean-squared displacement ratio
Statistics based on p variation
Straightness
Trappedness
D'Agostino-Pearson test statistic
Kolmogorov-Smirnov (KS) statistic against χ^2 distribution
Joseph exponent
Noah exponent
Moses exponent
Detrending moving average (DMA)
Average moving window characteristics
Maximum standard deviation

---

whereby each vth bin may show a distinct relationship of $P(n)$ with n. The width of this singularity spectrum, $\Delta\alpha = (\alpha_{\max} - \alpha_{\min})$, indicates the heterogeneity of these relationships [91,92].

Chhabra and Jensen's [89] method estimates $P(n)$ for N_n nonoverlapping windows of size n and transforms them into a "mass" $\mu(q)$ using a parameter q emphasizing higher or lower $P(n)$ for $q > 1$ and $q < 1$, respectively, in the form

$$\mu_v(q,n) = \frac{[P_v(n)]^q}{\sum_{j=1}^{N_n}[P_j(n)]^q}. \tag{6}$$

Then $\alpha(q)$ is the singularity for mass μ-weighted $P(n)$ estimated as

$$\alpha(q) = -\lim_{N_n \to \infty} \frac{1}{\log N_n} \sum_{v=1}^{N_n} \mu_v(q,n) \log P_v(n)$$

$$= \lim_{n \to 0} \frac{1}{\log n} \sum_{v=1}^{N_n} \mu_v(q,n) \log P_v(n). \tag{7}$$

Each estimated value of $\alpha(q)$ belongs to the multifractal spectrum only when the Shannon entropy of $\mu(q,n)$ scales with n according to the Hausdorff dimension $f(q)$ [89], where

$$f(q) = -\lim_{N_n \to \infty} \frac{1}{\log N_n} \sum_{v=1}^{N_n} \mu_v(q,n) \log \mu_v(q,n)$$

$$= \lim_{v \to 0} \frac{1}{\log n} \sum_{v=1}^{N_n} \mu_v(q,n) \log \mu_v(q,n). \tag{8}$$

For values of q yielding a strong relationship between Eqs. (7) and (8), as constituted by a minimum value r for the

TABLE II. MFS features utilized for anomalous diffusion classification. See also Fig. 2 to visualize the features.

MFS width of the original time series, $\Delta\alpha$
MFS width of the IAAFT surrogate time series, $\Delta\alpha_{\text{Surr}}$
Multifractal nonlinearity, $\mathcal{T}_{\text{MF}}$
Left-side width of the original spectrum, $\Delta\alpha_{\text{Left}}$
Right-side width of the original spectrum, $\Delta\alpha_{\text{Right}}$
Horizontal location of the singularity, $\alpha_{f(\alpha)=1}$
Height of the original spectrum, $\Delta f(\alpha)$
Left-side height of the original spectrum, $\Delta f(\alpha)_{\text{Left}}$
Right-size height of the original spectrum, $\Delta f(\alpha)_{\text{Right}}$
Difference in the left- and right-side height of the original spectrum, $\Delta f(\alpha)_{|\text{Left}-\text{Right}|}$
Mean of α values, $\overline{\alpha}$
Mean of $f(\alpha)$ values, $\overline{f(\alpha)}$
Number of points in the original spectrum, N_{Spec}

---

correlation coefficient, the parametric curve $\{\alpha(q), f(q)\}$ or $\{\alpha, f(\alpha)\}$ constitutes the multifractal spectrum and $\Delta\alpha$ (i.e., $\alpha_{\max} - \alpha_{\min}$) constitutes the multifractal spectrum width. The cutoff r determines that only scaling relationships of comparable strength can support the estimation of the multifractal spectrum, whether generated as cascades or surrogates. Using a correlation benchmark aims to operationalize previously raised concerns about misspecifications of the multifractal spectrum [93]. For each trajectory, we compute nine multifractal spectra $\{\alpha, f(\alpha)\}$, corresponding to all combinations of the scaling ranges of $N_{\max} \in \{N/4, N/8, N/16\}$, where N is the trajectory length, and the cutoff $r \in \{0.92, 0.95, 0.97\}$. In short, we systematically varied three different cutoffs of the correlation coefficient r and three maximum bin sizes. This approach allowed us to estimate multifractal features across a broad spectrum of precisions and coarse-grainings.

Our next objective was to discern whether a nonzero $\Delta\alpha$ truly signified multifractality arising from nonlinear interactions across various timescales. We compared $\Delta\alpha$ values between the original series and 32 iterated amplitude adjusted Fourier transform (IAAFT) surrogates [79,94] for each simulated series across generations 9 through 15. IAAFT stands out as a method capable of symmetrically reshuffling the original values around their autoregressive structure. Consequently, it generates surrogates that disentangle the phase ordering of spectral amplitudes within the series while preserving the linear temporal correlations. The one-sample $\mathcal{T}$ statistic, $\mathcal{T}_{\text{MF}}$, comes into play by computing the difference between $\Delta\alpha$ for the original series and the corresponding values for the 32 surrogates, which is then divided by the standard error of the spectrum width for these surrogates, facilitating a robust statistical assessment of multifractal nonlinearity.

Multifractal spectra are complex functions characterized by varying widths and heights across their two-dimensional definition, and they exhibit asymmetry and differing spacing across various ranges of the parameter q. To comprehensively capture the diverse aspects of these multifractal spectra, we incorporated various features spanning a wide range of characteristics. Specifically, we extracted nine features from multifractal spectra obtained for each trajectory, as listed in Table II and depicted in Fig. 2.
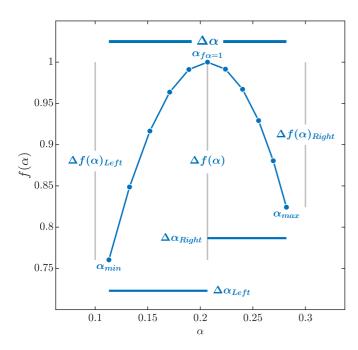
FIG. 2. Determining MFS features of anomalous diffusion trajectories. The multifractal spectrum of each trajectory was created by plotting the parametric curve $\{\alpha(q), f(q)\}$. $\alpha(q)$ is the singularity exponent and $f(q)$ the corresponding singularity dimension as defined in Eqs. (7) and (8).

D. ML classifiers

A neural network can essentially be described as a sophisticated function approximator. It aims to align its outputs, denoted as $f_\theta(X_i)$, with the actual target values, represented as $\hat{Y}_i$, based on the corresponding input data X_i [95,96]. In its simplest form, a neural network comprises multiple layers of neurons. Within each layer, the value of a neuron denoted as $O_{k,l}$ in layer l, is determined by the weighted sum of all neurons in the preceding layer, $O_{k,l-1}$, which is then passed through an activation function h,

$$O_{k',l} = h\left[\sum_k \theta_{k',k}^{(l)} \cdot O_{k,l-1} + \theta_{k',0}^{(l)}\right],\qquad(9)$$

where $\theta_{k',k}^{(l)}$ is the weight between neuron k' in the lth layer and neuron k in the $(l-1)$-th layer with $\theta_{k',0}^{(l)}$ as an additional offset. The output $f_\theta(X_i)$ of the neural network corresponds to the values of the neurons in the final layer, whereas the input X_i corresponds to the values of the neurons in the first layer.

The neural network's weights, collectively represented as θ, are derived by minimizing a loss function applied to a training dataset. Frequently, this loss function is the negative-log-likelihood loss [96],

$$\mathcal{L}_{\text{nll}} = -\sum_i \log p[\hat{Y}_i | f_\theta(X_i)],\qquad(10)$$

where $p[\hat{Y}_i | f_\theta(X_i)]$ is the probability the neural network assigned to the true target $\hat{Y}_i$ for input X_i. In classification tasks, we usually aim to predict discrete probabilities, denoted as $p_{i,k}$, about each class k as the true label for input X_i. In this context, the negative-log-likelihood is transformed into the
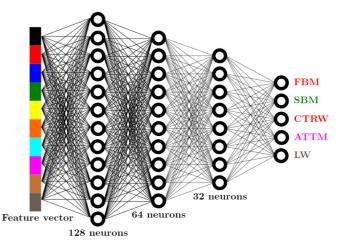

FIG. 3. Neural network architecture used for anomalous diffusion classification. A fully connected neural network was used with three hidden layers of size 128, 64, and 32 (or 256, 128, and 64 when using all additional features). The input layer comprised the (normalized) feature vector, with its dimension determined by the number of spectra used (13 features per spectrum). It incorporated an additional 26 or 39 features for the original or extended sets, respectively. The network then generated model scores for the five diffusion models examined.

well-known cross-entropy loss [97],

$$\mathcal{L}_{\text{cel}} = -\sum_{i,k} \hat{Y}_{i,k} \log(p_{i,k}),\qquad(11)$$

where $\hat{Y}_{i,k} = \delta_{j_i k}$ is a binary indicator of the true label j_i of input X_i.

The optimization of this loss function is accomplished through the utilization of stochastic gradient descent [98]. This study employed an advanced variant of stochastic gradient descent known as "Adaptive Moment Estimation" (Adam) [99]. In addition to Adam, we incorporated "stochastic weight averaging Gaussian" (SWAG)—which captures the uncertainty of the neural network's weight parameters, θ—toward the conclusion of the training process. This is achieved by fitting an approximate Gaussian distribution to the observed changes of θ during the gradient descent process. For in-depth insights into SWAG, we refer readers to Ref. [100], and for an application to anomalous diffusion to Ref. [72].

In contrast to the approach adopted in Ref. [72], where a recurrent neural network was utilized to classify anomalous diffusion models directly from raw positional data, the present study opted for a different strategy, focusing on extracted features, allowing us to employ a simpler neural network architecture. The used neural network comprised three hidden layers with dimensions 128, 64, and 32, utilizing the rectified linear unit [101] as the activation function, as visually represented in Fig. 3. This particular architecture was selected based on careful observation of the performance exhibited by multiple architectures throughout the training process and subsequent evaluation stages. Notably, when working with an extended feature set encompassing all the features outlined in Ref. [69], we observed that a more expansive network configuration yields benefits, thus opting for larger hidden-layer sizes of 256, 128, and 64. The network generates membership
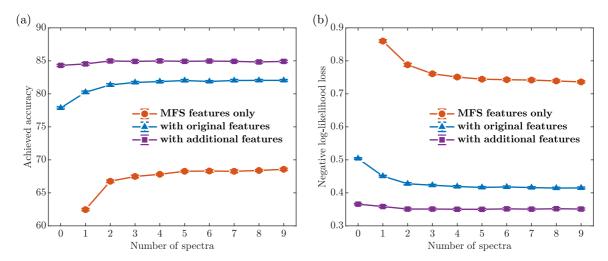
FIG. 4. Achieved accuracy (a) and loss (b) for anomalous diffusion classification using features from different numbers of multifractal spectra and feature combinations. The depicted error bars are obtained via subsampling on the test dataset.

scores for each of the five classes as a "logit vector," denoted as $Z_i = f_\theta(X_i)$, with values subsequently related to model probabilities $p_{i,k}$ through a normalized exponential (softmax) function [102],

$$p_{i,k} = \frac{\exp(z_{i,k})}{\sum_k \exp(z_{i,k})}. \tag{12}$$

To train the neural network, we conducted 300 epochs, during which we systematically shuffled the training dataset and divided it into batches of size 512. Each epoch constitutes one pass through the whole training dataset. The number of epochs was chosen so that including additional epochs did not lead to further improvement, even for the larger feature sets. The network weights are iteratively updated with each batch to minimize the loss function [as expressed in Eq. (4)], employing the *Adam* optimizer with a learning rate that decays from 10^{-3} to 10^{-4}. The final 20 epochs estimated SWAG, which entails determining a Gaussian probability density function on the network weights θ.

III. RESULTS

Our analysis began with assessing their stand-alone performance to evaluate the effectiveness of the newly introduced MFS features in ML-based classification. We gauged the achieved accuracy across varying numbers of spectra and delved into the significance of each feature. Considering that these MFS features may not individually rival state-of-the-art techniques, which often employ a wide array of features or operate directly on trajectory data, we explored an additional dimension. We investigated how the MFS features might enhance established feature sets by incorporating supplementary features inspired by Kowalek *et al.*'s work in Refs. [69,76] into our dataset. This encompassed the original feature set introduced in Ref. [76] and the enhanced extended feature set outlined in Ref. [69]. Furthermore, we organized the features into groups based on similar conceptual foundations for the extended feature set. This categorization enabled us to make meaningful performance comparisons by training ML

models on individual feature groups as an extension to the MFS features.

A. Classification performance with MFS features exclusively

We trained a neural network to predict the anomalous diffusion model exclusively based on the features extracted from multifractal spectra. To scrutinize the influence of spectrum selection, we employed various spectra, each comprising 13 distinct features, and documented the outcomes for the most promising combination of spectra. Figure 4 presents the attained accuracy and loss on the test dataset in relation to the number of spectra utilized; we only consider the graphs labeled as "MFS features only." In Fig. 4(a), the accuracy ranged from 62.5% to 68.6% based on the number of incorporated spectra. Notably, we observed a substantial surge in accuracy when transitioning from a single spectrum (62.5%) to two spectra (66.7%), but this improvement diminished as more spectra were included. A comparable pattern was observed in loss in Fig. 4(b), spanning from 0.860 to 0.736. It is worth noting that the loss function considers not only the predicted class but also the assigned probabilities for all five classes, as elucidated in Eq. (4). The diminished improvement observed with additional spectra is expected, given that these spectra stem from the same trajectories, albeit with slight parameter variations. Consequently, their inclusion contributes progressively less novel information as more spectra are added—indeed, augmenting the complexity of the neural network model did not yield improved performance when incorporating additional spectra.

Figures 5(a) and 5(b), respectively, present the confusion matrices for the models trained on features extracted from a single multifractal spectrum and features extracted from three multifractal spectra. These matrices illustrate the likelihood of the respective neural networks predicting each true class (rows) as one of the five classes (columns); therefore, the probabilities for correct predictions may be recovered from the diagonal entries. For comparison, Fig. 5(c) also shows the confusion matrix obtained when employing a state-of-the-art LSTM neural network, as introduced in Ref. [72],
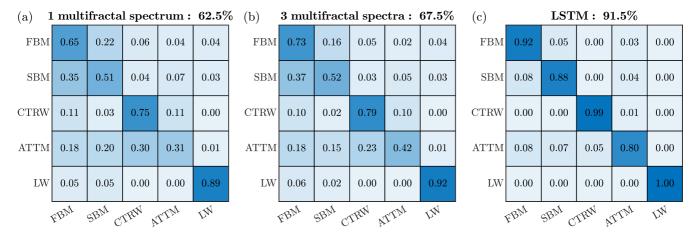
FIG. 5. Confusion matrices showing the accuracy of the anomalous diffusion classification using only the MFS features from just 1 spectrum (a) and 3 spectra (b), as well as for a state-of-the-art LSTM neural network trained on raw trajectories (c). The matrices show the probability of a ground-truth model on the vertical axis to be predicted as one of the models on the horizontal axis.

on the same dataset. The confusion matrices reveal that a network trained on a single spectrum [Fig. 5(a)] demonstrates proficiency in accurately identifying LW trajectories (89%) and CTRW trajectories (75%) but faces challenges in distinguishing between FBM (66%), SBM (50%), and particularly ATTM (31%). However, incorporating features from multiple spectra [Fig. 5(b)] significantly enhances performance for ATTM (42%) and FBM (73%), with noticeable, though less pronounced, improvements observed for all other models.

A notable advantage of feature-based ML, in contrast to non-feature-based approaches such as Bayesian deep learning [72], lies in its heightened interpretability. Specifically, these methods empower the identification of each feature's influence on the neural network's performance. For instance, one can selectively choose a feature, permute its position among the inputs and observe the resulting accuracy decrease attributable to this particular feature's misallocation. Tables III and IV present the permutation feature importance for models trained on singular or dual multifractal spectra, respectively. Notably, when utilizing a solitary spectrum (Table III), we discern the utmost significance for the right end of

the spectrum, denoted as $\Delta\alpha_{\mathrm{Right}}$ and $\Delta f(\alpha)_{\mathrm{Right}}$. A consistent pattern emerges across various scenarios, wherein the spatial orientation of the spectrum, as indicated by the singularity exponent α, outweighs the precise singularity dimension $f(\alpha)$ at those specific locations in terms of importance. The significance of features persists in the context of two spectra (Table IV), aligning with the observed behavior in the singular spectrum scenario. Slight enhancements in importance across most features are evident, indicative of an overall improved performance. Only $\Delta\alpha_{\mathrm{Left}}$ ascends from the fourth position in Table III to become the most crucial feature in Table IV—a shift suggesting that heterogeneity in $\Delta\alpha_{\mathrm{Left}}$ between them may assume heightened importance when leveraging multiple spectra.

Although achieving an accuracy from 62.5% to 68.6%, as we saw for the MFS features only in Fig. 4(a), is a notable improvement over random predictions (20% for predicting one out of five models), it does not reach the levels of performance attainable with state-of-the-art techniques developed

TABLE III. Permutation importance of the various MFS features obtained using only one multifractal spectrum.

Spectral feature	Permutation importance
$\Delta\alpha_{\mathrm{Right}}$	0.202
$\Delta f(\alpha)_{\mathrm{Right}}$	0.185
$\Delta\alpha$	0.174
$\Delta\alpha_{\mathrm{Left}}$	0.173
$\alpha_{f(\alpha)=1}$	0.139
$\Delta f(\alpha)_{|\mathrm{Left-Right}|}$	0.136
N_{Spec}	0.133
$\Delta f(\alpha)_{\mathrm{Left}}$	0.125
$\Delta\alpha_{\mathrm{Surr}}$	0.112
$\mathcal{T}_{\mathrm{MF}}$	0.059
$\overline{f(\alpha)}$	0.016
$\Delta f(\alpha)$	0.013
$\overline{\alpha}$	0.005

TABLE IV. Permutation importance of the various MFS features obtained using two multifractal spectra. The ranking of the MFS features stays mostly the same, except that the feature $\Delta\alpha_{\mathrm{Left}}$ moves up from fourth to the most important position.

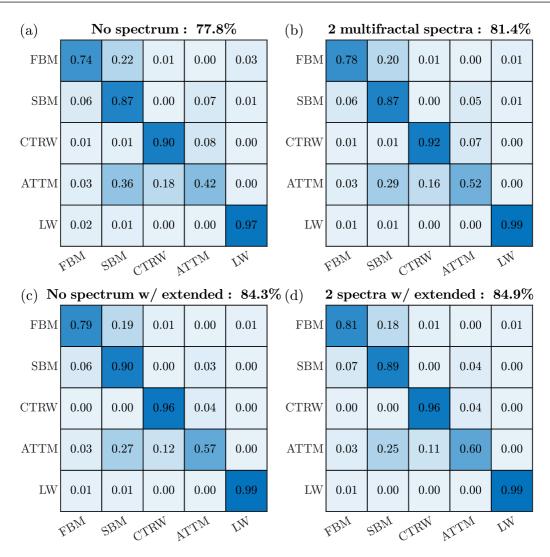| Spectral feature	Permutation importance
$\Delta\alpha_{\mathrm{Left}}$	0.215
$\Delta\alpha_{\mathrm{Right}}$	0.212
$\Delta f(\alpha)_{\mathrm{Right}}$	0.203
$\Delta\alpha$	0.185
$\alpha_{f(\alpha)=1}$	0.180
$\Delta f(\alpha)_{|\mathrm{Left-Right}|}$	0.164
N_{Spec}	0.159
$\Delta f(\alpha)_{\mathrm{Left}}$	0.147
$\Delta\alpha_{\mathrm{Surr}}$	0.141
$\mathcal{T}_{\mathrm{MF}}$	0.078
$\overline{f(\alpha)}$	0.021
$\Delta f(\alpha)$	0.015
$\overline{\alpha}$	0.005

FIG. 6. Confusion matrices showing the accuracy of the anomalous diffusion classification using MFS features and traditional features. The confusion matrices show the probability of a ground-truth model on the vertical axis to be predicted as one of the models on the horizontal axis. (a) Smaller feature set without any spectrum. (b) Smaller feature set with two multifractal spectra. (c) Extended feature set without any spectrum. (d) Extended feature set with two multifractal spectra.

during and after the AnDi-Challenge (e.g., Refs. [71–73]). This outcome aligns with expectations, given that our model relies solely on a single category of features. Notably, a model leveraging the features introduced in Refs. [69,76] demonstrated the ability to achieve an accuracy of 77.8%, which further increased to 84.3% when utilizing the extended feature set. Additionally, when employing the LSTM neural network from Ref. [72], which primarily operates on minimally preprocessed raw trajectories, we accomplished an accuracy of 91.7% using the same dataset as depicted in Fig. 5(c). Consequently, we proceed with our investigation to determine whether incorporating MFS features into established feature sets can improve classification performance.

B. Classification performance after adding MFS features to established feature sets

We next assessed the implications of augmenting the traditional feature sets, detailed in Sec. II B of Ref. [69], for classification performance, together with the recently introduced MFS features. Figure 4 showcases the attained accuracies and losses. The initial datapoint, representing no spectrum, delineates the classification performance without MFS features. In addition, we present the confusion matrices for the stand-alone traditional feature sets and their integration with MFS features from two spectra in Fig. 6. This comprehensive visualization provides insights into these distinct feature sets' comparative performance and interactions.

In the case of the smaller feature set—so-called original feature set, initially employed in Ref. [76], a discernible enhancement in accuracy is evident—from the initial 77.8% without MFS features to an elevated 82.0% with the inclusion of all nine spectra, as visible in the corresponding graph in Fig. 4(a). Notably, the influence of additional spectra diminishes rapidly, exhibiting no discernible changes surpassing random fluctuations beyond the inclusion of five spectra. A parallel pattern emerges for the loss [Fig. 4(b)], where a notable improvement— from 0.504 without spectra to 0.415 with all nine spectra—is observed. Although

TABLE V. Permutation importance for the top 10 features, combining two multifractal spectra with the original features as presented in Refs. [69,76]. Although the original features, primarily involving p variation and the anomalous exponent β, still exhibit the highest importance, they are closely followed by the new MFS features. Seven of the top 10 features have been derived from this newly introduced multifractal framework (highlighted in bold).

Feature	Permutation importance
p variation	0.294
α	0.195
$\mathbf{\Delta} f(\alpha)_{\mathrm{Right}}$	**0.117**
$\mathbf{\Delta}\alpha_{\mathrm{Right}}$	**0.109**
$\boldsymbol{\alpha}_{f(\alpha)=1}$	**0.098**
$\mathbf{\Delta}\alpha_{\mathrm{Left}}$	**0.094**
$\mathbf{\Delta}\alpha_{\mathrm{Surr}}$	**0.090**
Mean Gaussianity	0.080
$\mathbf{\Delta} f(\alpha)$	**0.076**
$\mathbf{\Delta}\alpha$	**0.075**

TABLE VI. Permutation importance for the top 10 features, combining two multifractal spectra with the original and extended features as presented in Ref. [69]. These results reveal that most of the top 10 features are the additional features introduced in Ref. [69]. Notably, two MFS features, $\alpha_{f(\alpha)=1}$ and $\Delta f(\alpha)_{\mathrm{Right}}$ (highlighted in bold), occupy the 9th and 10th positions in terms of importance, suggesting that while the newly introduced features may not be the most critical, they surpass several other traditional features present in anomalous diffusion in terms of importance.

Feature	Permutation importance
Moving window	0.248
p variation	0.184
Anomalous exponent	0.143
KS statistic against χ^2	0.127
Direct statistics	0.104
Maximum standard deviation	0.085
Joseph exponent	0.082
Mean Gaussianity	0.060
$\alpha_{f(\alpha)=1}$	0.058
$\Delta f(\alpha)_{\mathrm{Right}}$	0.054

the impact of additional spectra diminishes, the decline is not as abrupt as witnessed in the accuracy domain. Examining the confusion matrices in Figs. 6(a) and 6(b) unveils some intriguing insights. For instance, despite the models trained solely on MFS features exhibiting the weakest performance for ATTM, the most significant improvement is witnessed in the detection of ATTM, escalating from 42% [in Fig. 6(a)] to 52% [in Fig. 6(b)]. Subsequent enhancements are noted for FBM (from 74% to 78%), marginal gains for CTRW and LW (by 2%), and no measurable improvement for SBM.

Regarding the "extended" feature set [69], we observed a marginal yet perceptible uptick in accuracy—from an initial 84.3% to a refined 84.9% from the corresponding graph in Fig. 4(a). This suggests that most information encapsulated in the multifractal spectra may already exist within the extended feature set. Likewise, the loss in Fig. 4(b) exhibits a slight reduction, transitioning from 0.366 to 0.351. Including two-plus multifractal spectra had a minimal to negligible impact on loss and accuracy. Mirroring the trends observed in the smaller feature set, the confusion matrices presented in Figs. 6(c) and 6(d) showcase modest improvements for ATTM [ascending from 57% in Fig. 6(c) to 60% in Fig. 6(d)] and FBM (progressing from 79% to 81%), while the performance for the other three models remained relatively stable. This underscores the nuanced interplay between the extended feature set and MFS features in influencing model performance.

Tabels V and VI present feature-importance scores, largely aligning with the previously elucidated trends. These tables enumerate the top 10 features ranked by permutation importance for neural networks trained on the original or extended feature sets, incorporating MFS features from two spectra. It is pertinent to note that certain features, such as p variation, encompass multiple values collectively permuted for conciseness and are singularly represented with unified importance. Noteworthy prominence is accorded to the MFS features and the smaller feature set in Table V, with most of the top 10 comprising these novel elements. Interestingly, the original

features involving p varation and the anomalous exponent β claim the top two positions. Notable inclusions within the top 10 are the previously underrated features $\Delta\alpha_{\mathrm{Surr}}$, derived from surrogates, and $\Delta f(\alpha)$. This dynamic underscores the nuanced landscape of feature importance, shedding light on the distinctive contributions of the traditional and newly introduced features. Consistent with the diminished performance noted in the extended feature set, the MFS features assume a relatively lower level of importance in Table VI, signaling that a substantial portion of the information encapsulated in these new features might already be retrievable from the traditional feature set. Nevertheless, two specific MFS features—$\alpha_{f(\alpha)=1}$ and $\Delta f(\alpha)_{\mathrm{Right}}$—hold positions towards the tail end of the top 10 features, implying a heightened significance compared to several traditional features within the dataset.

To conclude our investigation, we systematically categorized the features within the extended feature set based on shared conceptual foundations. This organization enables a direct and meaningful comparison with the MFS feature group. The features were systematically grouped as listed in Table VII.

Finally, we trained an additional neural network with only the features within each designated group. We recorded the ensuing accuracies on the test set, as delineated in Table VIII. Except for the DMA, which failed to surpass the random-prediction accuracy of 20%, the remaining groups demonstrated classification performances within a comparable accuracy range of approximately 50–70%. Prominent among these groups were those harnessing the moving window characteristics (72.2%) and p varation (71.7%), securing the highest performance accuracies. Notably, the network fashioned from the MFS features extracted from three spectra closely trailed with an accuracy of 68.2%. Even the network trained solely on features from a singular multifractal spectrum showcased commendable performance, outpacing most other feature groups with an accuracy of 63%, except for the directedness measures, which achieved

TABLE VII. Traditional features organized into groups based on shared conceptual foundations. See Appendix B for detailed definitions of the features.

Concept group	Features
Features extracted from the time-averaged Mean-squared displacement (TAMSD)	Anomalous exponent Diffusion coefficient Mean-squared displacement ratio Trappedness
Statistics based on p variation	Scaling powers γ_p Monotonicity statistic P
Joseph, Noah, and Moses effect	Joseph exponent Noah exponent Moses exponent
Statistics based on comparison against the normal distribution	Kurtosis Mean Gaussianity D'Agostino-Pearson test statistic KS statistic against χ^2 distribution
Measures for the directedness of motion	Empirical velocity autocorrelation function Straightness Efficiency Fractal dimension
Detrending moving average	DMA
Moving window measures	Average moving window characteristics Maximum standard deviation
Measures to detect large jumps (excursions)	Maximal excursion Mean maximal excursion

an accuracy of 65.4%. These findings underscore the diverse efficacy of MFS features in contributing to the overall predictive capacity of the neural network in anomalous diffusion classification.

TABLE VIII. Achieved performance accuracies across various feature groupings reveal noteworthy distinctions. Feature sets derived from one or three multifractal spectra (highlighted in bold) emerged as among the most proficient, exhibiting only marginal performance differentials compared to the groups centered around p variation or moving window statistics (by 3.5–4%). These findings underscore the competitive performance of MFS features, positioning them close to other robust feature groupings in predictive efficacy.

Feature group	Achieved accuracy
Moving window	72.2%
p variation	71.7%
3 spectra	68.2%
Directedness measures	65.4%
1 spectrum	63.0%
vs normal	59.6%
Joseph, Noah, and Moses	58.1%
TAMSD	52.9%
Excursions	49.8%
DMA	20.0%

IV. DISCUSSION

We explored the potential of MFS features to discern effectively anomalous-diffusion trajectories originating from five prevalent models—FBM, SBM, CTRW, ATTM, and LW. To achieve this objective, we generated a dataset of 10^6 trajectories from these models, each yielding multiple—up to nine—multifractal spectra. Our study entailed a thorough analysis of neural network performance, incorporating features derived from varying numbers of spectra. Additionally, we systematically explored the augmentation of traditional feature datasets with multifractal spectra, enabling a comprehensive assessment of their impact. To facilitate a definitive comparison, we categorized features into concept groups, and neural networks were trained to utilize features from each designated group. The principal outcomes of these investigations are illustrated in Fig. 4 and tabulated in Table VIII.

Concretely, the subdivision of traditional features into two distinct sets—an older and a more comprehensive contemporary set has discerned a notable impact stemming from including new MFS features. This impact is particularly pronounced for the former set and remains discernibly measurable for the latter subset of our quantifiers, albeit of a lesser magnitude. Notably, methodologies based on the AnDi-Challenge, whether leveraging raw particle trajectories or a more exhaustive feature set, consistently outperform approaches reliant solely on MFS features. Nevertheless, on further investigation into the segmentation of traditional features into smaller conceptual groups, MFS features closely trailed the two top-performing quantifiers. These quantifiers, derived from moving-average and p variation statistics analyses, exhibited superior performance. Specifically, our analysis revealed a marginal reduction in accuracy for features derived from three spectra. At the same time, a comparatively more substantial decline in performance was observed for the less sensitive single-spectrum features (see entries highlighted in bold in Table VIII). Notably, the latter still outperformed several traditional features, exemplified by quantifiers comprising the Joseph, Moses, and Noah exponents. In summation, our findings underscore the diverse and potent efficacy of MFS features in augmenting the predictive capabilities of neural networks for classifying anomalous diffusion processes.

The multifractal formalism provides a set of parameters that are well suited to the ergodic causal modeling of anomalous diffusion processes. While traditional features, often employed in linear causal modeling [103–105], tend to disrupt ergodicity, multifractal descriptors, in contrast, exhibit ergodicity [78,106–109], thereby offering a dependable and consistent set of causal predictors [110–121]. The present finding that MFS features improved anomalous diffusion classification supports the growing interest in multifractal modeling within various fields of active matter. For example, in areas such as the dynamics of biomolecules within cells [122–125], the foraging behavior of wild animals [126–129], and the study of collective dynamics, including swarming and milling behaviors [112,130,131], multifractal formalisms have gained traction. The present finding underscores the significance of such approaches in these fields.

Notably, the frequently observed disruption of ergodicity in traditional features can serve as an advantage in model

classification. Unlike the current focus on individual trajectories, this approach necessitates access to a set of trajectories stemming from the same motion. By capturing the interplay between ensemble and time averages, such as through an amplitude scatter function, distinctions may arise based on the underlying diffusion model [132,133].

An intriguing avenue for further research lies in exploring alternative single-particle models that have not been explicitly addressed in the present investigation. Complex systems frequently manifest multiple dynamics in practical scenarios, presenting various facets of heterogeneities. These may include combinations of temporal variations in diffusivity, as evidenced in SBM, spatial heterogeneities, and correlated increments, as observed in FBM [134–136]. An investigation within this context would scrutinize the applicability of multifractal modeling to elucidate and characterize such intricate systems.

Interactions spanning diverse spatiotemporal scales can fundamentally reshape the backdrop for subsequent fluctuations. For instance, cascade-dynamical instabilities can generate turbulent structures, intricate patterns of motion where formerly parallel currents transform into a complex array of vortices and eddies, with intermittent surges and recessions throughout space and time [85,87,137] (see also Refs. [138,139]). Significantly, anomalous diffusion generating sometimes Lévy-like distributions distinguish active turbulence from its inertial counterpart [19,140]. The present finding that MFS features improved anomalous diffusion classification suggests a relationship between different diffusion coefficients and the specific geometries of the underlying fluctuations characterizing the observed data series. The intricate connection between multifractality and various models of anomalous diffusion is becoming increasingly evident, both from a theoretical [141–145] and empirical [128,129, 146–150] perspective. Multifractal formalisms and anomalous diffusion processes thus appear to be intricately intertwined, with their connection rooted in the far-from-equilibrium capacity to break time-reversal symmetry and to yield instead the multiscaled, nonlinear and multibody interactions characteristic of evolving living systems [151].

Multifractal formalisms represent an optimal analytical framework for ML-based classification of anomalous diffusion processes. Recent endeavors have encompassed Bayesian methodologies [58–62], various ML strategies [63–73], and even unsupervised techniques [74,75]. However, these approaches often rely on atheoretical features, which may not correspond to plausible generative mechanisms [73,76,77]. While these features have provided an intuitive way to model diffusion as a symmetric, homogeneous, ergodic spreading of probability mass, a potential problem with these features is that their heuristic value comes at the cost of model efficiency. Specifically, the raw empirical measurements of diffusive processes break ergodicity, suggesting very little homogeneity or symmetry and even less with larger samples. These features might not tame the ergodicity breaking and make modeling more effective. Rather, they are as likely to break ergodicity as the raw measurement series [106,108,152]. A more recent stream of diffusion modeling has begun to recognize that measured diffusive processes exhibit nested structure [122–125], strong context-sensitivity [126–129], and

emergent coordination patterns [112,130,131]. ML approaches might fail by using ill-suited features to describe nonergodic diffusive regimes. Multifractal-spectral features may provide a way to describe these heterogeneous diffusive processes explicitly, and the multifractal descriptors of such nonergodic processes are more likely to be ergodic [110–121]. Beyond the strictly heuristic value of intuitive linear features, multifractal-spectral features may afford ML approaches a dependable and consistent set of causal predictors.

While the primary focus of the statistical physics community has predominantly centered on the study of anomalous diffusion at the level of single-particle trajectories [10,153,154], a comprehensive investigation of biological processes implies the potential existence of multiple "particles," each exhibiting their distinct trajectories. Specifically, examining particle trajectories may have inspired existing models. Implicit in these models may have been their couching of particle behavior within shared, aggregate behavior in which the particle dynamics are sometimes only downstream effects of larger scale, ensemble behaviors. Hence, it is essential to recognize that shared constraints could influence the seemingly independent trajectories of these entities in ways that may not be readily discernible in linear spatiotemporal analysis. In this sense, the particle models reflect only a reduction of the behavior of a multiscaled architecture to a single point mass, that is, a lower-dimensional projection of a higher-dimensional system. The particle models thus carry this signature of high dimensionality.

Future research could elaborate single-particle-trajectory models towards network modeling of the ensemble to make the cascade-dynamical relationships more explicit (cf. Refs. [116,118,119,155]). This endeavor would aim to reconcile qualitative disparities among the particle models (i.e., among FBM, SBM, CTRW, ATTM, and LW) with the pervasive appearance [78] and emerging predictive capacity of multifractal structures within these models, suggesting a shared ancestry within a cascade-dynamical framework. The robust predictive capabilities of multifractal parameters in these models underscore the potential similarity in the underlying cascade dynamics, transcending the diversity of particle models. As such, multifractal modeling promises to unveil causal interactions among these trajectories. The proficiency in categorizing anomalous processes based on cascade-related features implies that ML algorithms may be able to classify trajectories stemming from a spectrum of cascade dynamics. This attempt could serve precise classification of higher-dimensional biological structures but also extend to biomedical applications, affording novel theoretical traction on the cascade-dynamical character of healthy and diseased biological and psychological systems [156–159], extending beyond single trajectories.

APPENDIX A: THEORETICAL MODELS

1. Fractional Brownian motion

In FBM, $x(t)$ is a Gaussian process with stationary increments; it is symmetric, $\langle x(t) \rangle = 0$, and importantly, its MSD scales as $\langle x(t) \rangle = 2K_H t^{2H}$, where H is the Hurst exponent and is related to the anomalous exponent β as $H = \beta/2$ [160–162]. The two-time correlation for FBM is $\langle x(t_1)x(t_2) \rangle = K_H(t_1^{2H} + t_2^{2H} - |t_1 - t_2|^{2H})$. FBM can also be defined as a process that arises from a generalized Langevin equation with nonwhite noise (or fractional Gaussian noise, FGN). The FGN has a standard normal distribution with zero mean and power-law correlation:

$$\langle \xi_{fGn}(t_1)\xi_{fGn}(t_2) \rangle = 2K_H H(2H - 1)|t_1 - t_2|^{2H-2}$$
$$+ 4K_H H|t_1 - t_2|^{2H-1}\delta(t_1 - t_2). \quad \text{(A1)}$$

The FBM features two regimes: one in which the noise is positively correlated ($1/2 < H < 1$, i.e., $1 < \beta < 2$, superdiffusive) and the other in which the noise is negatively correlated ($0 < H < 2$, i.e., $0 < \beta < 1$, subdiffusive). For $H = 1/2$ ($\beta = 1$), the noise is uncorrelated. Hence, the FBM converges to Brownian motion.

Various numerical approaches have been proposed to solve the FBM generalized Langevin equation. We use the method by Davies and Harte [163] (or Hosking [164] for H close to 1) via the fbm python package [165]. Details about the numerical implementations can be found in the associated reference.

2. Scaled Brownian motion

The SBM is a process described by the Langevin equation with a time-dependent diffusivity,

$$\frac{dx(t)}{dt} = \sqrt{2K(t)}\xi(t), \quad \text{(A2)}$$

where $\xi(t)$ is white Gaussian noise [166]. In the case when $K(t)$ has a power-law dependence on to t such that $K(t) = \beta K_\beta t^{\beta-1}$, MSD follows $< x^2(t) >_N = 2K_\beta t^\beta$. The numerical implementation of SBM is presented in Algorithm 1.

ALGORITHM 1. Generate SBM trajectory.

Input:
  length of the trajectory $T = N\Delta t$
  anomalous exponent β
Define:
  $\texttt{erfcinv}(\vec{a}) \rightarrow$ Inverse complementary error function of $\vec{a}$
  $U(N) \rightarrow$ returns N uniform random numbers $\in [0, 1]$
Calculate:
  $\vec{\Delta x} \leftarrow (t_2^\beta, t_3^\beta, \dots, t_N^\beta) - (t_1^\beta, t_2^\beta, \dots, t_{N-1}^\beta)$
  $\vec{\Delta x} \leftarrow \sqrt{2\vec{\Delta x}}\texttt{erfcinv}(2 - 2U(N-1))$
  $\vec{x} \leftarrow \text{cumsum}(\vec{\Delta x})$
Return: $\vec{x}$

---

3. Continuous-time random walk

The CTRW is a family of random walks with arbitrary displacement density. The waiting time between subsequent steps is a stochastic variable [167]. We considered a specific case of CTRW with waiting times following a power-law distribution $\psi(t) \propto t^{-\sigma}$ and displacements following a Gaussian distribution with variance D and zero means. In such case, the anomalous exponent is $\beta = \sigma - 1$ (MSD $= \langle x(t)^2 \rangle \propto t^\beta$). As the waiting times follow a power-law distribution, for $\sigma = 2$, MSD features Brownian motion with logarithmic corrections [168].

The numerical implementation of CTRW is presented in Algorithm 2. Notice that the variable τ represents the total time at ith iteration. The output vector $\vec{x}$ corresponds to the position of the particle at the irregular times given by $\vec{t}$.

ALGORITHM 2. Generate CTRW trajectory.

Input:
  length of the trajectory T
  anomalous exponent β
  diffusion coefficient D
Define:
  $\vec{x} \rightarrow$ empty vector
  $\vec{t} \rightarrow$ empty vector
  $N(\mu, S) \rightarrow$ Gaussian random number generator with mean μ and standard deviation S
  $i = 0; \tau = 0$
While $\tau < T$ **do**
  t_i sample randomly from $\psi(t) \sim t^{-\sigma}$
  $x_i \leftarrow x_{i-1} + N(0, \sqrt{D})$
  $\tau \leftarrow \tau + t_i$
  $i \leftarrow i + 1$
end while
Return: $\vec{x}, \vec{t}$

---

4. Annealed transient time motion

The ATTM implements the motion of a Brownian particle with time-dependent diffusivity [169]. The observable performs Brownian motion for a random time t_1 with a random diffusion coefficient D_1, then for t_2 with D_2, and so on. The diffusion coefficients follow a distribution such that $P(D) \propto D^{\sigma-1}$ with $\sigma > 0$ as $D \rightarrow 0$, and that decays rapidly for large D. If the random times t are sampled from a distribution with expected value $E[t|D] = D^{-\gamma}$, with $\sigma < \gamma < \sigma + 1$, the anomalous exponent is $\beta = \sigma/\gamma$. Here, we consider that the distribution is a delta function, $P_t(t|D) = \delta(t - D^{-\gamma})$. Hence, the time t_i in which the observable performs Brownian motion with a random diffusion coefficient D_i is $t_i = D_i^{-\gamma}$, with D_i extracted from $P(D)$.

The numerical implementation of ATTM is presented in Algorithm 3. In contrast to CTRW and LW, the only output is $\vec{x}$ because the trajectory is produced at regular intervals.

5. Lévy walk

The LW is a particular superdiffusive CTRW. Like subdiffusive CTRW, the flight time, that is, the time between

ALGORITHM 3. Generate ATTM trajectory.

Input:
  length of the trajectory T
  anomalous exponent β
  sampling time Δt
Define:
  While $\sigma > \gamma$ and $\gamma > \sigma + 1$ **do**
    $\sigma \leftarrow$ uniform random number $\in (0, 3]$
    $\gamma = \sigma / \beta$
  end while
  $\text{BM}(D_i, t_i, \Delta t) \rightarrow$ generates a Brownian motion trajectory of
  length t_i with diffusion coefficient D_i, sampled at time
  intervals Δt
While $\tau < T$ **do**
  $D_i \leftarrow$ sample randomly from $P(D) \propto D^{\sigma-1}$
  $t_i \leftarrow D_i^{-\gamma}$
  number of steps $N_i = \text{round}(t_i/\Delta t)$
  $x_i, \ldots, x_{i+N_i} \leftarrow \text{BM}(D_i, t_i, \Delta t)$
  $i \leftarrow i + N_i + 1$
  $\tau = \tau + N_i \Delta t$
end while
Return: $\vec{x}$

---

steps, for LW is irregular [170], but, in contrast to subdiffusive CTRW, the distribution of displacements for LW is not Gaussian. We considered the case in which the flight times follow the distribution $\psi(t) = t^{-\sigma-1}$. At each step, the displacement is Δx, and the step length is $|\Delta x|$. The displacements are correlated with the flight times such that the probability of moving a step Δx at time t and stopping at the new position to wait for a new random event to happen is $\psi(\Delta x, t) = \frac{1}{2}\delta(|\Delta x| - vt)\psi(t)$, where v is the velocity. The anomalous exponent is given by

$$\beta = \begin{cases} 2, & \text{if } 0 < \sigma < 1 \\ 3 - \sigma, & \text{if } 1 < \sigma < 2 \end{cases}. \tag{A1}$$

The numerical implementation of LW is presented in Algorithm 4. Notice that we use a random number r, which can take

values 0 or 1, to decide in which sense the step is performed. The output vectors $\vec{x}$ represent irregularly sampled positions and times.

ALGORITHM 4. Generate LW trajectory.

Input:
  length of the trajectory T
  anomalous exponent β
Define:
  $\vec{x} \rightarrow$ empty vector
  $\vec{t} \rightarrow$ empty vector
  $v \rightarrow$ random number $\in (0, 10)$
  $i = 0$
While $\tau < T$ **do**
  $t_i \leftarrow$ sample randomly from $\psi(t) \sim t^{-\sigma-1}$
  $x_i \leftarrow (-1)^r v t_i$, where random r is 0 or 1 with equal probability.
  $\tau \leftarrow \tau + t_i$
  $i \leftarrow i + 1$
end while
Return: $\vec{x}, \vec{t}$

APPENDIX B: TRADITIONAL FEATURES

This Appendix briefly introduces the definitions of the traditional features from Refs. [69,76] listed in Sec. II B.

1. Original features

a. Anomalous exponent

Four estimates for the anomalous diffusion exponent β constituted separate features:

(1) the standard estimation, based on fitting the empirical TAMSD to Eq. (1),

(2) three estimation methods proposed for trajectories with noise, which is normally distributed with zero mean [171],

    (a) using the estimator

$$\hat{\beta} = \frac{n_{\max} \sum_{n=1}^{n_{\max}} \log(n) \log[\langle \mathbf{r}^2(n\Delta t)\rangle] - \sum_{n=1}^{n_{\max}} \log(n)\left\{\sum_{n=1}^{n_{\max}} \log[\langle \mathbf{r}^2(n \cdot \Delta t)\rangle]\right\}}{n_{\max} \sum_{n=1}^{n_{\max}} \log^2(n) - \left[\sum_{n=1}^{n_{\max}} \log(n)\right]^2}, \tag{B1}$$

where n denotes time lag with $n_{\max} = N/10$—where N is $T/\Delta t$—rounded to the nearest lower integer (but not less than 4),

(b) simultaneous fitting of the parameters $\hat{D}$, $\hat{\beta}$, and $\hat{\sigma}$ in the relation

$$\langle \mathbf{r}^2(t)\rangle = 2d\hat{D}t^{\hat{\beta}} + \hat{\sigma}^2, \tag{B2}$$

where d denotes the embedding dimension, D is the diffusion coefficient, and σ^2 is the variance of noise,

(c) simultaneous fitting of the parameters $\hat{D}$ and $\hat{\beta}$ in the equation

$$\langle \mathbf{r}^2(n\Delta t)\rangle = 2d\hat{D}(n^{\hat{\beta}} - 1)(\Delta t)^{\hat{\beta}}. \tag{B2}$$

b. Diffusion coefficient

An estimator of the diffusion coefficient was extracted from the fit of the empirical TAMSD to Eq. (B2).

c. Efficiency

The efficiency E relates the net-squared displacement to the sum of squared step lengths,

$$E(N, 1) = \frac{|x_N - x_1|^2}{(N - 1)\sum_{i=1}^{N-1} |x_{i+1} - x_i|^2}. \tag{B4}$$

Efficiency ranges from 0 to 1 and should help detect directed motion, which takes values close to 1.

d. Empirical velocity autocorrelation function

The empirical velocity autocorrelation function [46] for lag 1 and point n is in one dimension,

$$\chi_n = \frac{1}{N-1-n} \sum_{i=1}^{N-1-n} (x_{i+1+n} - x_{i+n})(x_{i+1} - x_i), \quad \text{(B3)}$$

it can be used to distinguish different subdiffusive processes. In Ref. [69], χ_n for points $n = 1$ and $n = 2$ was used, as well as in the present study.

e. Fractal dimension

The fractal dimension measures the space-filling capacity of a pattern (a trajectory in our case). For a planar trajectory, it may be calculated as

$$D_f = \frac{\log N}{\log(NdL^{-1})}, \quad \text{(B4)}$$

where $L = \sum_i^N |\Delta x_i|$ is the total distance traveled, N is the number of steps, and d is the largest distance between any two positions [172]. It usually takes values around 1 for directed motion and around 2 for normal diffusion. For subdiffusive CTRW, it is also around 2, while for FBM, it is larger than 2.

f. Maximal excursion

The maximal excursion of the particle is

$$\text{ME} = \frac{\max_i(|x_{i+1} - x_i|)}{x_N - x_1}. \quad \text{(B5)}$$

It detects relatively long jumps (in comparison to the overall displacement).

g. Mean maximal excursion

The mean maximal excursion can replace the MSD as the observable used to determine the anomalous exponent [173]. It is defined as the standardized value of the largest distance traveled by a particle,

$$T_n = \frac{\max_i(|x_i - x_1|)}{\sqrt{\hat{\sigma}_N^2(t_N - t_1)}}. \quad \text{(B6)}$$

The parameter $\hat{\sigma}_N$ is a consistent estimator of the standard deviation,

$$\hat{\sigma}_N^2 = \frac{1}{2(N-1)\Delta t} \sum_{j=2}^{N} |x_j - x_{j-1}|^2. \quad \text{(B7)}$$

h. Mean Gaussianity

The Gaussianity $g(n)$ checks the Gaussian statistics of increments of a trajectory [174] as

$$g(n) = \frac{\langle r_n^4 \rangle}{3\langle r_n^2 \rangle^2} - 1, \quad \text{(B8)}$$

where $\langle r_n^k \rangle$ denotes the kth moment of the trajectory at time lag n. The Gaussianity for normal diffusion is equal to 0. The same result should be obtained for FBM since its increments follow a Gaussian distribution. Other types of motion should show deviations from that value.

Instead of looking at Gaussianities at single-time lags, in Ref. [69] and here, the mean Gaussianity across all lags was used as one of the features,

$$\langle g \rangle = \frac{1}{N} \sum_{i=1}^{N} g(n). \quad \text{(B9)}$$

i. Mean-squared displacement ratio

The MSD ratio gives information about the shape of the corresponding MSD curve. We will define it as

$$\text{MSDR}(n_1, n_2) = \frac{\langle r_{n_1}^2 \rangle}{\langle r_{n_2}^2 \rangle} - \frac{n_1}{n_2}, \quad \text{(B10)}$$

where $n_1 < n_2$. MSDR is zero for normal diffusion ($\beta = 1$). We should get MSDR $\leqslant 0$ for sub- and MSDR $\geqslant 0$ for superdiffusion. in Ref. [69] and the present study, $n_2 = n_1 + 1$ was taken, and then the averaged ratio across all $n_1 = 1, 2, \ldots, N - 1$ was calculated for every trajectory.

j. Kurtosis

The kurtosis gives insight into the asymmetry and peakedness of the distribution of points within a trajectory [175]. It is defined as the fourth moment,

$$K = \frac{1}{N} \sum_{i=1}^{N} \frac{(x_i - \bar{x})^4}{\sigma_x^4}, \quad \text{(B11)}$$

where $\bar{x}$ is the mean position and σ_x the standard deviation.

k. Statistics based on p varation

The empirical p varation is given by the formula [176]

$$V_m^{(p)} = \sum_{k=1}^{\frac{N}{m}-1} |x_{(k+1)m} - x_{km}|^p \propto m^{\gamma_p}. \quad \text{(B12)}$$

This statistic can be used to detect fractional Lévy stable motion (including FBM). Ten features based on $V_m^{(p)}$ were used for the classification of trajectories:

(1) the power γ_p fitted to p varation for lags 1 to 5 for nine values of p,

(2) the statistic P used in Ref. [77], based on the monotonicity changes of $V_m^{(p)}$ as a function of m as indicated by the sign of γ_p:

$$P = \begin{cases} 0 & \text{if } V_m^{(p)} \text{does not change the monotonicity}, \\ 1 & \text{if} \gamma_p \text{changes from negative to positive}, \\ -1 & \text{if} \gamma_p \text{changes from positive to negative}. \end{cases}$$

$$\text{(B13)}$$

l. Straightness

The straightness S measures the average direction change between subsequent steps. It relates the net displacement of a particle to the sum of all step lengths,

$$S = \frac{|x_N - x_1|}{\sum_{i=1}^{N-1} |x_{i+1} - x_i|}. \quad \text{(B14)}$$

m. Trappedness

The trappedness is the probability that a diffusing particle is trapped in a bounded region with radius r_0 up to some observation time t. [177] estimated this probability with

$$P(D, t, r_0) \approx 10^{0.2048 - 2.5117(Dt/r_0^2)}. \tag{B15}$$

r_0 is approximated by half of the maximum distance between any two positions along a given trajectory, D is estimated by fitting the first two points of the MSD curve (i.e., the so-called short-time diffusion coefficient), and t is chosen as the total observation time T.

2. Additional features

a. d'Agostino-Pearson test statistic

The d'Agostino-Pearson κ^2 test statistic [178] measures the departure of a given sample from normality,

$$\kappa^2 = Z_1(g_1) + Z_2(K), \tag{B16}$$

where K is the sample kurtosis given by Eq. (B11) and $g_1 = m_3/m_2^{3/2}$ is the sample skewness with m_j being the jth sample central moment. The transformations Z_1 and Z_2 bring the distributions of the skewness and kurtosis as close to the standard normal as possible. This feature must help distinguish SBM and ATTM from other trajectories.

b. Kolmogorov-Smirnov statistic against χ^2 distribution

The KS statistic quantifies the distance between the empirical distribution function of the sample $F_T(x)$ and the cumulative function $G_T(x)$ of a reference distribution,

$$D_T = \sup_x |F_T(x) - G_T(x)|. \tag{B17}$$

The next feature to consider is the statistic calculated by comparing the empirical distribution of squared increments from a trajectory to a sampled χ^2 distribution. This choice is rooted in the concept that a Gaussian trajectory should theoretically yield a distribution of squared increments closely resembling the χ^2 distribution.

c. Joseph, Noah, and Moses exponents

Processes featuring stationary increments can manifest anomalous scaling of MSD via two mechanisms that, in principle, defy the Gaussian central limit theorem. These mechanisms include long-time increment correlations, known as the Joseph effect, and a flat-tailed increment distribution, referred to as the Noah effect [179,180]. Notably, FBM typifies the first effect, while LW embodies the latter. Furthermore, nonstationary increment distributions can induce anomalous scaling, giving rise to the Moses effect [179]. The Moses effect plays a pivotal role in identifying SBM and ATTM trajectories.

All three effects may be quantified by exponents, which can be used as features. Given a stochastic process x_t and the corresponding increment process $\delta_t(\tau) = x_{t+\tau} - x_t$, the Joseph, Moses, and Noah exponents are defined as follows:

(1) The Joseph exponent J is estimated from the ensemble average of the rescaled range statistics,

$$\mathbb{E}\left[\frac{\max_{1 \leqslant i \leqslant n}[x_i - \frac{i}{n}x_n] - \min_{1 \leqslant i \leqslant n}[x_i - \frac{i}{n}x_n]}{\sigma_n}\right] \sim n^J, \tag{B18}$$

where σ_j is the standard deviation of the process x_j.

(2) The Moses exponent M is determined from the scaling of the ensemble probability distribution of the sum of the absolute value of the increments, which can be estimated by the scaling of the median of the probability distribution of $Y_n = \sum_{i=1}^n |\delta_i|$,

$$\mathbb{E}[Y_n] \sim n^{M + \frac{1}{2}}. \tag{B19}$$

(3) The Noah exponent L is extracted from the scaling of the ensemble probability distribution of the sum of squared increments, which can be estimated by the scaling of the median of the probability distribution of $Z_n = \sum_{i=1}^n \delta_i^2$:

$$\mathbb{E}[Z_n] \sim n^{2L + 2M - 1}. \tag{B20}$$

The {J,M,L} exponents are related to the anomalous exponent β, [32,181]

$$\beta/2 = J + M + L - 1. \tag{B21}$$

d. Detrending moving average

The DMA statistic [182] is given by

$$\text{DMA}(\tau) = \frac{1}{N - \tau} \sum_{i=\tau+1}^{N} (x_i - \bar{x}_i^\tau)^2, \tag{B22}$$

for $\tau = \{1, 2, \ldots\}$, where $\bar{x}_i^\tau$ is a moving average of τ observations, that is, $\bar{x}_i^\tau = \frac{1}{\tau+1} \sum_{j=0}^{\tau} x_{i-j}$. According to Ref. [182], a DMA-based statistical test can help detect SBM. In Ref. [69] and in this work, DMA(1) and DMA(2) were used as features.

e. Average moving window characteristics

Let us define the following moving window characteristic:

$$\text{MW}_m = \frac{1}{2(N - m - 2)} \sum_{t=1}^{N-m-2} \left| \text{sgn}\left[\bar{x}_{t+2}^{(m)} - \bar{x}_{t+1}^{(m)}\right] \right.$$
$$\left. - \text{sgn}\left[\bar{x}_{t+1}^{(m)} - \bar{x}_t^{(m)}\right] \right|, \tag{B23}$$

where $\bar{x}^{(m)}$ denotes a statistic of the process calculated within the window of length m and sgn is the sign function. We here use four attributes calculating MW_m using the mean and standard deviation for $\bar{x}$ with windows of lengths $m = 10$ and $m = 20$.

f. Maximum standard deviation

The last two features from the extended feature set rely on the standard deviation σ_m of the process calculated within windows of length m,

$$\text{MXM}_m = \frac{\min[\sigma_m(t)]}{\max[\sigma_m(t)]} \tag{B24}$$

and

$$\mathrm{MXC}_m = \frac{\max |\sigma_m(t+1) - \sigma_m(t)|}{\sigma}, \qquad \text{(B25)}$$

where σ denotes the sample standard deviation over the whole trajectory and $\sigma_m(t)$ the standard deviation within the window starting at t and ending at $t + m\Delta t$. We used $m = 3$. These features must improve the detection of ATTM-type movements.

[1] Y. Sagi, M. Brook, I. Almog, and N. Davidson, Observation of anomalous diffusion and fractional self-similarity in one dimension, Phys. Rev. Lett. **108**, 093002 (2012).

[2] J. Zhao, Q. Deng, S. M. Avdoshenko, L. Fu, J. Eckert, and M. H. Rümmeli, Direct in situ observations of single Fe atom catalytic processes and anomalous diffusion at graphene edges, Proc. Natl. Acad. Sci. USA **111**, 15641 (2014).

[3] D. S. Banks and C. Fradin, Anomalous diffusion of proteins due to molecular crowding, Biophys. J. **89**, 2960 (2005).

[4] E. Barkai, Y. Garini, and R. Metzler, Strange kinetics of single molecules in living cells, Phys. Today **65**, 29 (2012).

[5] G. Guigas and M. Weiss, Sampling the cell with anomalous diffusion-The discovery of slowness, Biophys. J. **94**, 90 (2008).

[6] F. Höfling and T. Franosch, Anomalous transport in the crowded world of biological cells, Rep. Prog. Phys. **76**, 046602 (2013).

[7] J.-H. Jeon, V. Tejedor, S. Burov, E. Barkai, C. Selhuber-Unkel, K. Berg-Sørensen, L. Oddershede, and R. Metzler, *In vivo* anomalous diffusion and weak ergodicity breaking of lipid granules, Phys. Rev. Lett. **106**, 048103 (2011).

[8] J.-H. Jeon, Hector Martinez-Seara Monne, M. Javanainen, and R. Metzler, Anomalous diffusion of phospholipids and cholesterols in a lipid bilayer and its origins, Phys. Rev. Lett. **109**, 188103 (2012).

[9] D. Krapf and R. Metzler, Strange interfacial molecular dynamics, Phys. Today **72**(9), 48 (2019).

[10] R. Metzler and J. Klafter, The random walk's guide to anomalous diffusion: A fractional dynamics approach, Phys. Rep. **339**, 1 (2000).

[11] K. Ritchie, X.-Y. Shan, J. Kondo, K. Iwasawa, T. Fujiwara, and A. Kusumi, Detection of non-Brownian diffusion in the cell membrane in single molecule tracking, Biophys. J. **88**, 2266 (2005).

[12] I. M. Tolić-Nørrelykke, E.-L. Munteanu, G. Thon, L. Oddershede, and K. Berg-Sørensen, Anomalous diffusion in living yeast cells, Phys. Rev. Lett. **93**, 078102 (2004).

[13] T. E. Angelini, E. Hannezo, X. Trepat, M. Marquez, J. J. Fredberg, and D. A. Weitz, Glass-like dynamics of collective cell migration, Proc. Natl. Acad. Sci. USA **108**, 4714 (2011).

[14] P. Dieterich, R. Klages, R. Preuss, and A. Schwab, Anomalous dynamics of cell migration, Proc. Natl. Acad. Sci. USA **105**, 459 (2008).

[15] P. Dieterich, O. Lindemann, M. L. Moskopp, S. Tauzin, A. Huttenlocher, R. Klages, A. Chechkin, and A. Schwab, Anomalous diffusion and asymmetric tempering memory in neutrophil chemotaxis, PLoS Comput. Biol. **18**, e1010089 (2022).

[16] I. Golding and E. C. Cox, Physical nature of bacterial cytoplasm, Phys. Rev. Lett. **96**, 098102 (2006).

[17] S. Hapca, J. W. Crawford, and I. M. Young, Anomalous diffusion of heterogeneous populations characterized by normal diffusion at the individual level, J. R. Soc. Interface **6**, 111 (2009).

[18] A. Lagarde, N. Dagès, T. Nemoto, V. Démery, D. Bartolo, and T. Gibaud, Colloidal transport in bacteria suspensions: From bacteria collision to anomalous and enhanced diffusion, Soft Matter **16**, 7503 (2020).

[19] S. Mukherjee, R. K. Singh, M. James, and S. S. Ray, Anomalous diffusion and Lévy walks distinguish active from inertial turbulence, Phys. Rev. Lett. **127**, 118001 (2021).

[20] S. Petrovskii and A. Morozov, Dispersal in a statistically structured population: Fat tails revisited, Am. Natural. **173**, 278 (2009).

[21] S. Benhamou, How many animals really do the Lévy walk? Ecology **88**, 1962 (2007).

[22] A. James, M. J. Plank, and A. M. Edwards, Assessing Lévy walks as models of animal foraging, J. R. Soc. Interface **8**, 1233 (2011).

[23] A. M. Reynolds and C. J. Rhodes, The Lévy flight paradigm: Random search patterns and mechanisms, Ecology **90**, 877 (2009).

[24] C. T. Brown, L. S. Liebovitch, and R. Glendon, Lévy flights in Dobe Ju/'hoansi foraging patterns, Hum. Ecol. **35**, 129 (2007).

[25] D. A. Raichlen, B. M. Wood, A. D. Gordon, A. Z. Mabulla, F. W. Marlowe, and H. Pontzer, Evidence of lévy walk foraging patterns in human hunter–gatherers, Proc. Natl. Acad. Sci. USA **111**, 728 (2014).

[26] A. G. Cherstvy, D. Vinod, E. Aghion, I. M. Sokolov, and R. Metzler, Scaled geometric Brownian motion features sub-or superexponential ensemble-averaged, but linear time-averaged mean-squared displacements, Phys. Rev. E **103**, 062127 (2021).

[27] V. Plerou, P. Gopikrishnan, L. A. Nunes Amaral, X. Gabaix, and H. E. Stanley, Economic fluctuations and anomalous diffusion, Phys. Rev. E **62**, R3023(R) (2000).

[28] A. Vázquez, J. G. Oliveira, Z. Dezsö, K.-I. Goh, I. Kondor, and A.-L. Barabási, Modeling bursts and heavy tails in human dynamics, Phys. Rev. E **73**, 036127 (2006).

[29] F. A. Oliveira, R. M. Ferreira, L. C. Lapas, and M. H. Vainstein, Anomalous diffusion: A basic mechanism for the evolution of inhomogeneous systems, Front. Phys. **7**, 18 (2019).

[30] I. M. Sokolov and J. Klafter, From diffusion to anomalous diffusion: A century after Einstein's Brownian motion, Chaos **15**, 026103 (2005).

[31] S. F. Timashev, Y. S. Polyakov, P. I. Misurkin, and S. G. Lakeev, Anomalous diffusion as a stochastic component in the dynamics of complex processes, Phys. Rev. E **81**, 041128 (2010).

[32] O. Vilk, E. Aghion, T. Avgar, C. Beta, O. Nagel, A. Sabri, R. Sarfati, D. K. Schwartz, M. Weiss, D. Krapf *et al.*, Unravelling the origins of anomalous diffusion: From molecules to migrating storks, Phys. Rev. Res. **4**, 033055 (2022).

[33] A. V. Weigel, B. Simon, M. M. Tamkun, and D. Krapf, Ergodic and nonergodic processes coexist in the plasma membrane as observed by single-molecule tracking, Proc. Natl. Acad. Sci. USA **108**, 6438 (2011).

[34] R. Brown, XXVII. A brief account of microscopical observations made in the months of June, July and August 1827, on the particles contained in the pollen of plants; and on the general existence of active molecules in organic and inorganic bodies, Philos. Mag. **4**, 161 (1828).

[35] A. Einstein, Über die von der molekularkinetischen theorie der wärme geforderte bewegung von in ruhenden flüssigkeiten suspendierten teilchen, Ann. Phys. **322**, 549 (1905).

[36] A. Bancaud, S. Huet, N. Daigle, J. Mozziconacci, J. Beaudouin, and J. Ellenberg, Molecular crowding affects diffusion and binding of nuclear proteins in heterochromatin and reveals the fractal organization of chromatin, EMBO J. **28**, 3785 (2009).

[37] J.-P. Bouchaud and A. Georges, Anomalous diffusion in disordered media: Statistical mechanisms, models and physical applications, Phys. Rep. **195**, 127 (1990).

[38] I. Bronstein, Y. Israel, E. Kepten, S. Mai, Y. Shav-Tal, E. Barkai, and Y. Garini, Transient anomalous diffusion of telomeres in the nucleus of mammalian cells, Phys. Rev. Lett. **103**, 018102 (2009).

[39] A. Caspi, R. Granek, and M. Elbaum, Enhanced diffusion in active intracellular transport, Phys. Rev. Lett. **85**, 5655 (2000).

[40] A. D. Fernández, P. Charchar, A. G. Cherstvy, R. Metzler, and M. W. Finnis, The diffusion of doxorubicin drug molecules in silica nanoslits is non-Gaussian, intermittent and anticorrelated, Phys. Chem. Chem. Phys. **22**, 27955 (2020).

[41] F. Höfling, K.-U. Bamberg, and T. Franosch, Anomalous transport resolved in space and time by fluorescence correlation spectroscopy, Soft Matter **7**, 1358 (2011).

[42] J.-H. Jeon, M. Javanainen, H. Martinez-Seara, R. Metzler, and I. Vattulainen, Protein crowding in lipid bilayers gives rise to non-Gaussian anomalous lateral diffusion of phospholipids and proteins, Phys. Rev. X **6**, 021006 (2016).

[43] M. J. Saxton, Anomalous subdiffusion in fluorescence photobleaching recovery: A Monte Carlo study, Biophys. J. **81**, 2226 (2001).

[44] G. Seisenberger, M. U. Ried, T. Endress, H. Buning, M. Hallek, and C. Brauchle, Real-time single-molecule imaging of the infection pathway of an adeno-associated virus, Science **294**, 1929 (2001).

[45] P. R. Smith, I. E. Morrison, K. M. Wilson, N. Fernandez, and R. J. Cherry, Anomalous diffusion of major histocompatibility complex class I molecules on HeLa cells determined by single particle tracking, Biophys. J. **76**, 3331 (1999).

[46] S. C. Weber, A. J. Spakowitz, and J. A. Theriot, Bacterial chromosomal loci move subdiffusively through a viscoelastic cytoplasm, Phys. Rev. Lett. **104**, 238102 (2010).

[47] M. Weiss, Single-particle tracking data reveal anticorrelated fractional Brownian motion in crowded fluids, Phys. Rev. E **88**, 010101(R) (2013).

[48] D. Arcizet, B. Meier, E. Sackmann, J. O. Rädler, and D. Heinrich, Temporal analysis of active and passive transport in living cells, Phys. Rev. Lett. **101**, 248103 (2008).

[49] A. Caspi, R. Granek, and M. Elbaum, Diffusion and directed motion in cellular transport, Phys. Rev. E **66**, 011916 (2002).

[50] M. de Jager, F. J. Weissing, P. M. Herman, B. A. Nolet, and J. van de Koppel, Lévy walks evolve through interaction between movement and environmental complexity, Science **332**, 1551 (2011).

[51] M. H. G. Duits, Y. Li, S. A. Vanapalli, and F. Mugele, Mapping of spatiotemporal heterogeneous particle dynamics in living cells, Phys. Rev. E **79**, 051910 (2009).

[52] M. C. Gonzalez, C. A. Hidalgo, and A.-L. Barabasi, Understanding individual human mobility patterns, Nature (London) **453**, 779 (2008).

[53] F. Leoni and G. Franzese, Structural behavior and dynamics of an anomalous fluid between attractive and repulsive walls: Templating, molding, and superdiffusion, J. Chem. Phys. **141**, 174501 (2014).

[54] A. Mashanova, T. H. Oliver, and V. A. Jansen, Evidence for intermittency and a truncated power law from highly resolved aphid movement data, J. R. Soc. Interface **7**, 199 (2010).

[55] P. G. Meyer, A. G. Cherstvy, H. Seckler, R. Hering, N. Blaum, F. Jeltsch, and R. Metzler, Directedness, correlations, and daily cycles in springbok motion: From data via stochastic models to movement prediction, Phys. Rev. Res. **5**, 043129 (2023).

[56] R. Nathan, W. M. Getz, E. Revilla, M. Holyoak, R. Kadmon, D. Saltz, and P. E. Smouse, A movement ecology paradigm for unifying organismal movement research, Proc. Natl. Acad. Sci. USA **105**, 19052 (2008).

[57] A. Ott, J.-P. Bouchaud, D. Langevin, and W. Urbach, Anomalous diffusion in "living polymers:" A genuine Levy flight? Phys. Rev. Lett. **65**, 2201 (1990).

[58] J. Krog and M. A. Lomholt, Bayesian inference with information content model check for Langevin equations, Phys. Rev. E **96**, 062106 (2017).

[59] J. Krog, L. H. Jacobsen, F. W. Lund, D. Wüstner, and M. A. Lomholt, Bayesian model selection with fractional Brownian motion, J. Stat. Mech.: Theory Exp. (2018) 093501.

[60] S. Park, S. Thapa, Y. Kim, M. A. Lomholt, and J.-H. Jeon, Bayesian inference of Lévy walks via hidden Markov models, J. Phys. A: Math. Theor. **54**, 484001 (2021).

[61] S. Thapa, M. A. Lomholt, J. Krog, A. G. Cherstvy, and R. Metzler, Bayesian analysis of single-particle tracking data using the nested-sampling algorithm: Maximum-likelihood model selection applied to stochastic-diffusivity data, Phys. Chem. Chem. Phys. **20**, 29018 (2018).

[62] S. Thapa, S. Park, Y. Kim, J.-H. Jeon, R. Metzler, and M. A. Lomholt, Bayesian inference of scaled versus fractional Brownian motion, J. Phys. A: Math. Theor. **55**, 194003 (2022).

[63] S. Bo, F. Schmidt, R. Eichhorn, and G. Volpe, Measurement of anomalous diffusion using recurrent neural networks, Phys. Rev. E **100**, 010102(R) (2019).

[64] F. Cichos, K. Gustavsson, B. Mehlig, and G. Volpe, Machine learning for active matter, Nat. Mach. Intell. **2**, 94 (2020).

[65] M. Gajowczyk and J. Szwabiński, Detection of anomalous diffusion with deep residual networks, Entropy **23**, 649 (2021).

[66] A. Gentili and G. Volpe, Characterization of anomalous diffusion classical statistics powered by deep learning (CONDOR), J. Phys. A: Math. Theor. **54**, 314003 (2021).

[67] N. Granik, L. E. Weiss, E. Nehme, M. Levin, M. Chein, E. Perlson, Y. Roichman, and Y. Shechtman, Single-particle diffusion characterization by deep learning, Biophys. J. **117**, 185 (2019).

[68] J. Janczura, P. Kowalek, H. Loch-Olszewska, J. Szwabiński, and A. Weron, Classification of particle trajectories in living cells: Machine learning versus statistical testing hypothesis for fractional anomalous diffusion, Phys. Rev. E **102**, 032402 (2020).

[69] P. Kowalek, H. Loch-Olszewska, Ł. Łaszczuk, J. Opała, and J. Szwabiński, Boosting the performance of anomalous diffusion classifiers with the proper choice of features, J. Phys. A: Math. Theor. **55**, 244005 (2022).

[70] G. Muñoz-Gil, M. A. Garcia-March, C. Manzo, J. D. Martín-Guerrero, and M. Lewenstein, Single trajectory characterization via machine learning, New J. Phys. **22**, 013010 (2020).

[71] G. Muñoz-Gil, G. Volpe, M. A. Garcia-March, E. Aghion, A. Argun, C. B. Hong, T. Bland, S. Bo, J. A. Conejero, N. Firbas *et al.*, Objective comparison of methods to decode anomalous diffusion, Nat. Commun. **12**, 6253 (2021).

[72] H. Seckler and R. Metzler, Bayesian deep learning for error estimation in the analysis of anomalous diffusion, Nat. Commun. **13**, 6717 (2022).

[73] H. Seckler, J. Szwabiński, and R. Metzler, Machine-learning solutions for the analysis of single-particle diffusion trajectories, J. Phys. Chem. Lett. **14**, 7910 (2023).

[74] J. Pineda, B. Midtvedt, H. Bachimanchi, S. Noé, D. Midtvedt, G. Volpe, and C. Manzo, Geometric deep learning reveals the spatiotemporal fingerprint ofmicroscopic motion, Nat. Mach. Intell. **5**, 71 (2023).

[75] G. Muñoz-Gil, G. G. i Corominas, and M. Lewenstein, Unsupervised learning of anomalous diffusion data an anomaly detection approach, J. Phys. A: Math. Theor. **54**, 504001 (2021).

[76] P. Kowalek, H. Loch-Olszewska, and J. Szwabiński, Classification of diffusion modes in single-particle tracking data: Feature-based versus deep-learning approach, Phys. Rev. E **100**, 032410 (2019).

[77] H. Loch-Olszewska and J. Szwabiński, Impact of feature choice on machine learning classification of fractional anomalous diffusion, Entropy **22**, 1436 (2020).

[78] M. Mangalam, R. Metzler, and D. G. Kelty-Stephen, Ergodic characterization of nonergodic anomalous diffusion processes, Phys. Rev. Res. **5**, 023144 (2023).

[79] E. A. F. E. Ihlen, Introduction to multifractal detrended fluctuation analysis in Matlab, Front. Physiol. **3**, 141 (2012).

[80] D. G. Kelty-Stephen, K. Palatinus, E. Saltzman, and J. A. Dixon, A tutorial on multifractality, cascades, and interactivity for empirical time series in ecological science, Ecol. Psychol. **25**, 1 (2013).

[81] D. G. Kelty-Stephen, E. Lane, L. Bloomfield, and M. Mangalam, Multifractal test for nonlinearity of interactions across scales in time series, Behav. Res. Methods **55**, 2249 (2023).

[82] S. Ritschel, A. G. Cherstvy, and R. Metzler, Universality of delay-time averages for financial time series: Analytical results, computer simulations, and analysis of historical stock-market prices, J. Phys.: Complex. **2**, 045003 (2021).

[83] D. Vinod, A. G. Cherstvy, W. Wang, R. Metzler, and I. M. Sokolov, Nonergodicity of reset geometric Brownian motion, Phys. Rev. E **105**, L012106 (2022).

[84] W. Wang, A. G. Cherstvy, R. Metzler, and I. M. Sokolov, Restoring ergodicity of stochastically reset anomalous-diffusion processes, Phys. Rev. Res. **4**, 013161 (2022).

[85] B. B. Mandelbrot, Intermittent turbulence in self-similar cascades: Divergence of high moments and dimension of the carrier, J. Fluid Mech. **62**, 331 (1974).

[86] D. Schertzer, S. Lovejoy, F. Schmitt, Y. Chigirinskaya, and D. Marsan, Multifractal cascade dynamics and turbulent intermittency, Fractals **05**, 427 (1997).

[87] M. F. Shlesinger, B. J. West, and J. Klafter, Lévy dynamics of enhanced diffusion: Application to turbulence, Phys. Rev. Lett. **58**, 1100 (1987).

[88] G. Muñoz, H. Bachimanchi, J. Pineda, B. Midtvedt, M. Lewenstein, R. Metzler, D. Krapf, G. Volpe, and C. Manzo, Quantitative evaluation of methods to analyze motion changes in single-particle experiments, arXiv:2311.18100 (2023).

[89] A. Chhabra and R. V. Jensen, Direct determination of the f(α) singularity spectrum, Phys. Rev. Lett. **62**, 1327 (1989).

[90] B. B. Mandelbrot and B. B. Mandelbrot, *The Fractal Geometry of Nature* (WH Freeman, New York, NY, 1982), Vol. 1.

[91] T. C. Halsey, M. H. Jensen, L. P. Kadanoff, I. Procaccia, and B. I. Shraiman, Fractal measures and their singularities: The characterization of strange sets, Phys. Rev. A **33**, 1141 (1986).

[92] B. B. Mandelbrot, *Fractals and Scaling in Finance: Discontinuity, Concentration, Risk* (Springer, New York, 2013).

[93] M. Zamir, Critique of the test of multifractality as applied to biological data, J. Theor. Biol. **225**, 407 (2003).

[94] T. Schreiber and A. Schmitz, Improved surrogate data for nonlinearity tests, Phys. Rev. Lett. **77**, 635 (1996).

[95] L. V. Fausett, *Fundamentals of Neural Networks: Architectures, Algorithms and Applications* (Prentice Hall, Hoboken, NJ, 1994).

[96] E. Alpaydin, *Introduction to Machine Learning* (MIT Press, Cambridge, MA, 2020).

[97] Z. Zhang and M. Sabuncu, Generalized cross entropy loss for training deep neural networks with noisy labels, Adv. Neural Inf. Process. Syst. **31**, 8792 (2018).

[98] L. Bottou, Large-scale machine learning with stochastic gradient descent, in *Proceedings of COMPSTAT'2010: 19th International Conference on Computational Statistics* (Springer, Berlin, 2010), pp. 177–186.

[99] D. P. Kingma and J. Ba, Adam: A method for stochastic optimization, arXiv:1412.6980 (2014).

[100] W. J. Maddox, P. Izmailov, T. Garipov, D. P. Vetrov, and A. G. Wilson, A simple baseline for bayesian uncertainty in deep learning, in *Advances in Neural Information Processing Systems* (MIT Press, Cambridge, MA, 2019), Vol. 32.

[101] R. H. Hahnloser, R. Sarpeshkar, M. A. Mahowald, R. J. Douglas, and H. S. Seung, Digital selection and analogue amplification coexist in a cortex-inspired silicon circuit, Nature (Lond.) **405**, 947 (2000).

[102] B. Gao and L. Pavel, On the properties of the softmax function with application in game theory and reinforcement learning, arXiv:1704.00805 (2017).

[103] S. Kian-Bostanabad and M.-R. Azghani, The relationship between RMS electromyography and thickness change in the skeletal muscles, Med. Eng. Phys. **43**, 92 (2017).

[104] J. Vink, M. Westover, A. Pascual-Leone, and M. Shafi, EEG functional connectivity predicts propagation of TMS-evoked potentials, Brain Stimul. **10**, 516 (2017).

[105] J. J. Vink, D. C. Klooster, R. A. Ozdemir, M. B. Westover, A. Pascual-Leone, and M. M. Shafi, EEG functional connectivity is a weak predictor of causal brain interactions, Brain Topogr. **33**, 221 (2020).

[106] D. G. Kelty-Stephen and M. Mangalam, Fractal and multifractal descriptors restore ergodicity broken by non-Gaussianity in time series, Chaos Solitons Fract. **163**, 112568 (2022).

[107] D. G. Kelty-Stephen and M. Mangalam, Multifractal descriptors ergodically characterize non-ergodic multiplicative cascade processes, Physica A **617**, 128651 (2023).

[108] M. Mangalam and D. G. Kelty-Stephen, Ergodic descriptors of non-ergodic stochastic processes, J. R. Soc. Interface **19**, 20220095 (2022).

[109] M. Mangalam, A. Sadri, J. Hayano, E. Watanabe, K. Kiyono, and D. G. Kelty-Stephen, Multifractal foundations of biomarker discovery for heart disease and stroke, Sci. Rep. **13**, 18316 (2023).

[110] L. Bloomfield, E. Lane, M. Mangalam, and D. G. Kelty-Stephen, Perceiving and remembering speech depend on multifractal nonlinearity in movements producing and exploring speech, J. R. Soc. Interface **18**, 20210272 (2021).

[111] C. R. Booth, H. L. Brown, E. G. Eason, S. Wallot, and D. G. Kelty-Stephen, Expectations on hierarchical scales of discourse: Multifractality predicts both short-and long-range effects of violating gender expectations in text reading, Discourse Process. **55**, 12 (2018).

[112] N. S. Carver, D. Bojovic, and D. G. Kelty-Stephen, Multifractal foundations of visually-guided aiming and adaptation to prismatic perturbation, Hum. Move. Sci. **55**, 61 (2017).

[113] J. A. Dixon, J. G. Holden, D. Mirman, and D. G. Stephen, Multifractal dynamics in the emergence of cognitive structure, Top. Cogn. Sci. **4**, 51 (2012).

[114] N. Jacobson, Q. Berleman-Paul, M. Mangalam, D. G. Kelty-Stephen, and C. Ralston, Multifractality in postural sway supports quiet eye training in aiming tasks: A study of golf putting, Hum. Move. Sci. **76**, 102752 (2021).

[115] D. G. Kelty-Stephen and J. A. Dixon, Interwoven fluctuations during intermodal perception: Fractality in head sway supports the use of visual feedback in haptic perceptual judgments by manual wielding, J. Exp. Psychol. Hum. Percept. Perform. **40**, 2289 (2014).

[116] D. G. Kelty-Stephen, I. C. Lee, N. S. Carver, K. M. Newell, and M. Mangalam, Multifractal roots of suprapostural dexterity, Hum. Move. Sci. **76**, 102771 (2021).

[117] M. Mangalam, R. Chen, T. R. McHugh, T. Singh, and D. G. Kelty-Stephen, Bodywide fluctuations support manual exploration: Fractal fluctuations in posture predict perception of heaviness and length via effortful touch by the hand, Hum. Move. Sci. **69**, 102543 (2020).

[118] M. Mangalam, N. S. Carver, and D. G. Kelty-Stephen, Global broadcasting of local fractal fluctuations in a bodywide distributed system supports perception via effortful touch, Chaos Solitons Fract. **135**, 109740 (2020).

[119] M. Mangalam, N. S. Carver, and D. G. Kelty-Stephen, Multifractal signatures of perceptual processing on anatomical sleeves of the human body, J. R. Soc. Interface **17**, 20200328 (2020).

[120] M. Mangalam and D. G. Kelty-Stephen, Multiplicative-cascade dynamics supports whole-body coordination for perception via effortful touch, Hum. Move. Sci. **70**, 102595 (2020).

[121] S. Wallot and D. G. Kelty-Stephen, Interaction-dominant causation in mind and brain, and its implication for questions of generalization and replication, Minds Mach. **28**, 353 (2018).

[122] N. Cardenas, S. Kumar, and S. Mohanty, Dynamics of cellular response to hypotonic stimulation revealed by quantitative phase microscopy and multi-fractal detrended fluctuation analysis, Appl. Phys. Lett. **101**, 203702 (2012).

[123] S. Chaieb, Š. Málková, and J. Lal, Why the wrinkling transition in partially polymerized membranes is not universal? Fractal-multifractal hierarchy, J. Theor. Biol. **251**, 60 (2008).

[124] V. Rezania, F. C. Sudirga, and J. A. Tuszynski, Multifractality nature of microtubule dynamic instability process, Physica A **573**, 125929 (2021).

[125] A. Wawrzkiewicz-Jałowiecka, P. Trybek, B. Dworakowska, and Ł. Machura, Multifractal properties of BK channel currents in human glioblastoma cells, J. Phys. Chem. B **124**, 2382 (2020).

[126] E. D. Gutiérrez and J. L. Cabrera, A neural coding scheme reproducing foraging trajectories, Sci. Rep. **5**, 18009 (2015).

[127] Y. Ikeda, P. Jurica, H. Kimura, H. Takagi, Z. R. Struzik, K. Kiyono, Y. Arata, and Y. Sako, *C. elegans* episodic swimming is driven by multifractal kinetics, Sci. Rep. **10**, 14775 (2020).

[128] F. G. Schmitt and L. Seuront, Multifractal random walk in copepod behavior, Physica A **301**, 375 (2001).

[129] L. Seuront and H. E. Stanley, Anomalous diffusion and multifractality enhance mating encounters in the ocean, Proc. Natl. Acad. Sci. USA **111**, 2206 (2014).

[130] V. Balaban, S. Lim, G. Gupta, J. Boedicker, and P. Bogdan, Quantifying emergence and self-organisation of *Enterobacter cloacae* microbial communities, Sci. Rep. **8**, 12416 (2018).

[131] H. Koorehdavoudi, P. Bogdan, G. Wei, R. Marculescu, J. Zhuang, R. W. Carlsen, and M. Sitti, Multi-fractal characterization of bacterial swimming dynamics: A case study on real and simulated *Serratia marcescens*, Proc. Roy. Soc. A: Math. Phys. Eng. Sci. **473**, 20170154 (2017).

[132] J.-H. Jeon and R. Metzler, Analysis of short subdiffusive time series: Scatter of the time-averaged mean-squared displacement, J. Phys. A: Math. Theor. **43**, 252001 (2010).

[133] J.-H. Jeon, A. V. Chechkin, and R. Metzler, Scaled Brownian motion: A paradoxical process with a time dependent diffusivity for the description of anomalous diffusion, Phys. Chem. Chem. Phys. **16**, 15811 (2014).

[134] A. G. Cherstvy and R. Metzler, Ergodicity breaking, ageing, and confinement in generalized diffusion processes with position and time dependent diffusivity, J. Stat. Mech.: Theory Exp. (2015) P05010.

[135] W. Wang, A. G. Cherstvy, X. Liu, and R. Metzler, Anomalous diffusion and nonergodicity for heterogeneous diffusion processes with fractional Gaussian noise, Phys. Rev. E **102**, 012146 (2020).

[136] W. Wang, R. Metzler, and A. G. Cherstvy, Anomalous diffusion, aging, and nonergodicity of scaled Brownian motion with

fractional Gaussian noise: Overview of related experimental observations and models, Phys. Chem. Chem. Phys. **24**, 18482 (2022).

[137] S. Lovejoy, D. Schertzer, and P. Silas, Diffusion in one-dimensional multifractal porous media, Water Resour. Res. **34**, 3283 (1998).

[138] M. Mangalam, A. D. Likens, and D. G. Kelty-Stephen, Multifractal nonlinearity as a robust estimator of multiplicative cascade dynamics, arXiv:2312.05653 (2023).

[139] M. Mangalam and D. G. Kelty-Stephen, Multifractal emergent processes: Multiplicative interactions override nonlinear component properties, arXiv:2401.05105 (2024).

[140] A. G. Cherstvy, W. Wang, R. Metzler, and I. M. Sokolov, Inertia triggers nonergodicity of fractional Brownian motion, Phys. Rev. E **104**, 024115 (2021).

[141] V. V. Afanasiev, R. Z. Sagdeev, and G. M. Zaslavsky, Chaotic jets with multifractal space-time random walk, Chaos **1**, 143 (1991).

[142] W. Chen, H. Sun, X. Zhang, and D. Korošak, Anomalous diffusion modeling by fractal and fractional derivatives, Comput. Math. Appl. **59**, 1754 (2010).

[143] J.-R. de Dreuzy, P. Davy, J. Erhel, and J. de Brémond d'Ars, Anomalous diffusion exponents in continuous two-dimensional multifractal media, Phys. Rev. E **70**, 016306 (2004).

[144] L. Gmachowski, Fractal model of anomalous diffusion, Eur. Biophys. J. **44**, 613 (2015).

[145] S. C. Lim and S. V. Muniandy, Self-similar Gaussian processes for modeling anomalous diffusion, Phys. Rev. E **66**, 021114 (2002).

[146] D. R. Bickel, Simple estimation of intermittency in multifractal stochastic processes: Biomedical applications, Phys. Lett. A **262**, 251 (1999).

[147] S. Lovejoy and D. Schertzer, *The Weather and Climate: Emergent Laws and Multifractal Cascades* (Cambridge University Press, Cambridge, MA, 2018).

[148] R. Menu and T. Roscilde, Anomalous diffusion and localization in a positionally disordered quantum spin array, Phys. Rev. Lett. **124**, 130604 (2020).

[149] L. Seuront, F. G. Schmitt, M. C. Brewer, J. R. Strickler, and S. Souissi, From random walk to multifractal random walk in zooplankton swimming behavior, Zool. Stud. **43**, 498 (2004).

[150] A. Sharifi-Viand, M. Mahjani, and M. Jafarian, Investigation of anomalous diffusion and multifractal dimensions in polypyrrole film, J. Electroanal. Chem. **671**, 51 (2012).

[151] M. R. Shaebani, A. Wysocki, R. G. Winkler, G. Gompper, and H. Rieger, Computational models for active matter, Nat. Rev. Phys. **2**, 181 (2020).

[152] M. Mangalam and D. G. Kelty-Stephen, Point estimates, simpson's paradox, and nonergodicity in biological sciences, Neurosci. Biobehav. Rev. **125**, 98 (2021).

[153] R. Metzler and J. Klafter, The restaurant at the end of the random walk: Recent developments in the description of anomalous transport by fractional dynamics, J. Phys. A: Math. Gen. **37**, R161 (2004).

[154] R. Metzler, J.-H. Jeon, A. G. Cherstvy, and E. Barkai, Anomalous diffusion models and their properties: Non-stationarity, non-ergodicity, and ageing at the centenary of single particle tracking, Phys. Chem. Chem. Phys. **16**, 24128 (2014).

[155] D. G. Stephen, W.-H. Hsu, D. Young, E. L. Saltzman, K. G. Holt, D. J. Newman, M. Weinberg, R. J. Wood, R. Nagpal, and E. C. Goldfield, Multifractal fluctuations in joint angles during infant spontaneous kicking reveal multiplicativity-driven coordination, Chaos Solitons Fract. **45**, 1201 (2012).

[156] A. Humeau, F. Chapeau-Blondeau, D. Rousseau, P. Rousseau, W. Trzepizur, and P. Abraham, Multifractality, sample entropy, and wavelet analyses for age-related changes in the peripheral cardiovascular system: Preliminary results, Med. Phys. **35**, 717 (2008).

[157] A. L. Goldberger, L. A. Amaral, J. M. Hausdorff, P. C. Ivanov, C.-K. Peng, and H. E. Stanley, Fractal dynamics in physiology: Alterations with disease and aging, Proc. Natl. Acad. Sci. USA **99**, 2466 (2002).

[158] J. Suckling, A. M. Wink, F. A. Bernard, A. Barnes, and E. Bullmore, Endogenous multifractal brain dynamics are modulated by age, cholinergic blockade and cognitive performance, J. Neurosci. Methods **174**, 292 (2008).

[159] B. J. West, M. Latka, M. Glaubic-Latka, and D. Latka, Multifractality of cerebral blood flow, Physica A **318**, 453 (2003).

[160] J.-H. Jeon and R. Metzler, Fractional Brownian motion and motion governed by the fractional Langevin equation in confined geometries, Phys. Rev. E **81**, 021103 (2010).

[161] A. N. Kolmogorov, The wiener spiral and some other interesting curves in Hilbert space, Doklady Akademii Nauk SSSR **26**, 115 (1940).

[162] B. B. Mandelbrot and J. W. Van Ness, Fractional Brownian motions, fractional noises and applications, SIAM Rev. **10**, 422 (1968).

[163] R. B. Davies and D. S. Harte, Tests for Hurst effect, Biometrika **74**, 95 (1987).

[164] J. R. Hosking, Modeling persistence in hydrological time series using fractional differencing, Water Resour. Res. **20**, 1898 (1984).

[165] A. T. Wood and G. Chan, Simulation of stationary Gaussian processes in $[0, 1]^d$, J. Comput. Graph. Stat. **3**, 409 (1994).

[166] G. Muñoz-Gil, C. Romero-Aristizabal, N. Mateos, F. Campelo, L. I. de Llobet Cucalon, M. Beato, M. Lewenstein, M. F. Garcia-Parajo, and J. A. Torreno-Pina, Stochastic particle unbinding modulates growth dynamics and size of transcription factor condensates in living cells, Proc. Natl. Acad. Sci. USA **119**, e2200667119 (2022).

[167] H. Scher and E. W. Montroll, Anomalous transit-time dispersion in amorphous solids, Phys. Rev. B **12**, 2455 (1975).

[168] J. Klafter and I. M. Sokolov, *First Steps in Random Walks: From Tools to Applications* (Oxford University Press, Oxford, UK, 2011).

[169] P. Massignan, C. Manzo, J. A. Torreno-Pina, M. F. García-Parajo, M. Lewenstein, and G. J. Lapeyre, Jr., Nonergodic subdiffusion from Brownian motion in an in homogeneous medium, Phys. Rev. Lett. **112**, 150603 (2014).

[170] J. Klafter and G. Zumofen, Lévy statistics in a Hamiltonian system, Phys. Rev. E **49**, 4873 (1994).

[171] Y. Lanoiselée, G. Sikora, A. Grzesiek, D. S. Grebenkov, and A. Wyłomańska, Optimal parameters for anomalous-diffusion-exponent estimation from noisy data, Phys. Rev. E **98**, 062139 (2018).

[172] M. J. Katz and E. B. George, Fractals and the analysis of growth paths, Bull. Math. Biol. **47**, 273 (1985).

[173] V. Tejedor, O. Bénichou, R. Voituriez, R. Jungmann, F. Simmel, C. Selhuber-Unkel, L. B. Oddershede, and R. Metzler, Quantitative analysis of single particle trajectories: Mean maximal excursion method, Biophys. J. **98**, 1364 (2010).

[174] D. Ernst, J. Köhler, and M. Weiss, Probing the type of anomalous diffusion with single-particle tracking, Phys. Chem. Chem. Phys. **16**, 7686 (2014).

[175] J. A. Helmuth, C. J. Burckhardt, P. Koumoutsakos, U. F. Greber, and I. F. Sbalzarini, A novel supervised trajectory segmentation algorithm identifies distinct types of human adenovirus motion in host cells, J. Struct. Biol. **159**, 347 (2007).

[176] K. Burnecki and A. Weron, Fractional Lévy stable motion can model subdiffusive dynamics, Phys. Rev. E **82**, 021130 (2010).

[177] M. J. Saxton, Lateral diffusion in an archipelago. Single-particle diffusion, Biophys. J. **64**, 1766 (1993).

[178] R. d'Agostino and E. S. Pearson, Tests for departure from normality. empirical results for the distributions of b^2 and $\sqrt{b^1}$, Biometrika **60**, 613 (1973).

[179] E. Aghion, P. G. Meyer, V. Adlakha, H. Kantz, and K. E. Bassler, Moses, Noah and Joseph effects in Lévy walks, New J. Phys. **23**, 023002 (2021).

[180] B. B. Mandelbrot and J. R. Wallis, Noah, Joseph, and operational hydrology, Water Resour. Res. **4**, 909 (1968).

[181] L. Chen, K. E. Bassler, J. L. McCauley, and G. H. Gunaratne, Anomalous scaling of stochastic processes and the Moses effect, Phys. Rev. E **95**, 042141 (2017).

[182] M. Balcerek, K. Burnecki, G. Sikora, and A. Wyłomańska, Discriminating Gaussian processes via quadratic form statistics, Chaos **31**, 063101 (2021).